Journal of Physics and Chemistry of Solids 170 (2022) 110875

Contents lists available at ScienceDirect

Journal of Physics and Chemistry of Solids

journal homepage: www.elsevier.com/locate/jpcs

# Synthesis of ultrathin, nano-sized $Ti_3C_2T_x$ with abundant =O and –OH terminals and high transparency as a cocatalyst: Enabling design of high-performance Titania-$Ti_3C_2T_x$ hybrid photocatalysts

Ahmed Al Mayyahi [a], Swagotom Sarker [a], Brian M.Everhart [a], Bade Tonyali [b], Umut Yucel [b], Placidus B Amama [a,*]

[a] Tim Taylor Department of Chemical Engineering, Kansas State University, Manhattan, KS, 66506, USA
[b] Department of Animal Sciences and Industry, Kansas State University, Manhattan, KS, 66506, USA

ARTICLE INFO

*Keywords:*
Hybrid photocatalysts
$TiO_2$
MXene
Cocatalyst
Gas and liquid phase reactions

ABSTRACT

Conventional $Ti_3C_2T_x$ used in photocatalysis usually has properties that are detrimental to the process such as thick layers, a micro-sized structure with low transparency, and a high concentration of fluorine terminals. Herein, we demonstrate the synthesis of ultrathin, nano-sized $Ti_3C_2T_x$ with abundant oxygen-containing groups (=O and –OH) and high transparency (designated as N–$Ti_3C_2T_x$) as an alternative cocatalyst in liquid and gas phase photocatalysis. N–$Ti_3C_2T_x$ is prepared by a two-step process that involves etching Al from $Ti_3AlC_2$ via fluorine treatment followed by simultaneous exfoliation and fluorine reduction. N–$Ti_3C_2T_x$ is then coupled with $TiO_2$ via hydration and dehydration approaches to form a photocatalyst ($TiO_2$–N–$Ti_3C_2T_x$) with distinct morphology and surface chemistry. The small size of N–$Ti_3C_2T_x$ facilitates a strong interfacial contact with $TiO_2$, thereby enhancing electron transport between $TiO_2$ and N–$Ti_3C_2T_x$, and electron-hole separation; and (2) the high transparency of N–$Ti_3C_2T_x$ facilitates photon-$TiO_2$ interactions. As a consequence, the photocatalytic activity of $TiO_2$–N–$Ti_3C_2T_x$ is superior to that of pristine $TiO_2$, $TiO_2$ coupled with thin, micro-sized $Ti_3C_2T_x$ that is characterized by low transparency and fluorine terminals, and the widely used $Ti_3C_2T_x$-based photocatalyst synthesized by thermal nucleation of $TiO_2$ on $Ti_3C_2T_x$. The high photocatalytic activity of $TiO_2$–N–$Ti_3C_2T_x$ is also attributed to the presence of abundant = O and –OH terminals on N–$Ti_3C_2T_x$ that boosts pollutant adsorption. The study provides a rational approach for coupling $TiO_2$ and $Ti_3C_2T_x$ to promote beneficial charge transfer properties and synergistic effects that have far-reaching applications in photocatalysis.

## 1. Introduction

Two-dimensional transition metal carbides and nitrides, known as MXenes, have received immense attention since their discovery at Drexel University in 2011 [1]. The general formula of MXenes is $M_{n+1}X_nT_n$, where M is early transition metal, X is carbon or nitrogen, and T is surface functional terminals (= O, –OH, and/or –F). The most widely used MXene is titanium carbide ($Ti_3C_2T_x$) and is characterized by unique properties that are of massive benefit to photocatalysis: (1) high mobility of charge carriers that can promote migration and separation of photoexcited electron-hole pairs [2], (2) Ti sites on $Ti_3C_2T_x$ surface that may provide stronger redox reactivity compared to the traditional carbon material [3], and (3) unique surface chemistry of $Ti_3C_2T_x$ represented by its hydrophilic nature and abundant functional terminals that can adsorb a variety of molecules and ionic species [4,5]. The distinctive properties of $Ti_3C_2T_x$ highlighted have impelled the design of $Ti_3C_2T_x$-based photocatalysts with the aim of increasing mobility of the charge carriers, reactant adsorption, and surface reactivity. In this regard, numerous $Ti_3C_2T_x$-based photocatalysts such as BiOBr–$Ti_3C_2T_x$, CdS–$Ti_3C_2T_x$, $Ag_3PO_4$–$Ti_3C_2T_x$, $RuO_2$–$TiO_2$–$Ti_3C_2T_x$, g–$C_3N_4$–$Ti_3C_2T_x$ and $CuFe_2O_4$–$Ti_3C_2T_x$ have been designed and employed in various applications including water splitting, $O_2$ production, $N_2$ fixation, and bacterial inactivation [6–12].

Hybrids formed by coupling $Ti_3C_2T_x$ and $TiO_2$ have emerged as a promising family of environmental photocatalysts, in which the resulting Schottky junction formed between them leads to effective separation of photo-generated electron-hole pairs, while the presence of functional terminals on $Ti_3C_2T_x$ (particularly, =O and –OH groups) facilitates

* Corresponding author.
*E-mail address:* pamama@ksu.edu (P. B Amama).

https://doi.org/10.1016/j.jpcs.2022.110875
Received 15 April 2022; Received in revised form 20 June 2022; Accepted 25 June 2022
Available online 4 July 2022

pollutant adsorption and degradation on the catalyst surface. One approach that has been utilized to synthesize $TiO_2$–$Ti_3C_2T_x$ hybrid is the nucleation of $TiO_2$ nanoparticles on $Ti_3C_2T_x$ surface through thermal treatment. The hybrids produced by oxidation of $Ti_3C_2T_x$ at elevated temperatures (160–800 °C) have shown noticeable performance in photocatalytic degradation of environmental pollutants [13–18]. However, the conversion of a Ti layer into $TiO_2$ sacrifices the structural integrity of $Ti_3C_2T_x$ and possibly reduces its ability to accept the photogenerated charges, undermining the benefit of utilizing $Ti_3C_2T_x$ in photocatalysis. As an alternative approach, coupling commercial $TiO_2$ with thin/layered, micro-sized $Ti_3C_2T_x$ through hydration and dehydration has been used to produce $TiO_2$–$Ti_3C_2T_x$ hybrid while preserving the structural integrity of $Ti_3C_2T_x$ [4]. However, the average size of $Ti_3C_2T_x$ used (several hundred nanometers to a few micrometers) in coupling is significantly larger than that of $TiO_2$ nanoparticles (typically in the range of 20–200 nm). This considerable size difference can diminish the quality of interfacial contact formed between $TiO_2$ and $Ti_3C_2T_x$, and in turn, impede the mobility of charge carriers in the hybrid structure. Also, light transmittance of $Ti_3C_2T_x$ is linearly dependent on its thickness that decreases with the number of layers and is independent of wavelength. For instance, a transmittance of 68% was attained by a 17-nm thin film of $Ti_3C_2T_x$, indicating 32% of incident light was absorbed or scattered [19,20]. The photon interaction with the semiconductor ($TiO_2$ nanoparticles) is a critical first step in photocatalysis as it yields the reactive oxygen species; therefore, a cocatalyst that potentially obstructs penetration of photons to $TiO_2$ is undesired. Furthermore, the conventional $Ti_3C_2T_x$ used in photocatalysis is typically terminated by fluorine groups that are inevitably attached to the surface during the fabrication process. These terminals are undesired in photocatalysis as they mitigate the adsorption of pollutants on the surface of MXene-based photocatalysts [4,21–23]. For the full potential of $Ti_3C_2T_x$-based photocatalysts to be realized, the aforementioned challenges that are directly connected to the photocatalytic process would have to be addressed.

A recent study reveals that ultrathin MXene ($Ti_3C_2T_x$ film with thickness of less than 2.5 nm) possesses a transmittance of 90% while returning high conductivity exceeding 6500 S $cm^{-1}$ [24]. Also, a previous investigation involving the coupling of $TiO_2$ and graphene suggests utilizing a nano-sized graphitic structure as opposed to a micro-sized one as it maximizes the interfacial contact and promotes electron-hole separation [25]. Hence, it is reasonable to hypothesize that coupling ultrathin, nanosized $Ti_3C_2T_x$ and $TiO_2$ has the potential to maximize the interfacial contact in $Ti_3C_2T_x$-$TiO_2$ photocatalysts and promote migration and separation of charge carriers without interrupting photon flux to $TiO_2$. Therefore, herein, we demonstrate synthesis of ultrathin, nano-sized $Ti_3C_2T_x$ (N–$Ti_3C_2T_x$) that is characterized by high transparency and abundant = O and –OH groups (reduced fluorine content), and subsequent coupling with $TiO_2$ to produce a hybrid photocatalyst (designated as $TiO_2$–N–$Ti_3C_2T_x$). The photocatalytic activity of the photocatalysts was evaluated in liquid phase via methylene blue (MB) degradation and in gas phase via $NO_x$ oxidation. Our results reveal the superior photocatalytic activity of $TiO_2$–N–$Ti_3C_2T_x$ in comparison to pristine $TiO_2$ and $TiO_2$ coupled with thin, micro-sized $Ti_3C_2T_x$ ($TiO_2$-M-$Ti_3C_2T_x$) that is characterized by low transparency and fluorine terminals on the surface. Comprehensive morphological, optical, and chemical characterization of the photocatalysts has enabled elucidation of the observed differences in photocatalytic activity. Our findings will benefit current efforts aimed at exploiting the outstanding properties of MXenes in the design of efficient hybrid photocatalysts.

## 2. Experimental section

### 2.1. Synthesis of M-$Ti_3C_2T_x$ and N–$Ti_3C_2T_x$

The reaction between HCl and LiF was exploited to etch Al from MAX phase ($Ti_3AlC_2$) and exfoliate the sheets to produce M-$Ti_3C_2T_x$ [26,27]. 1 g of LiF (Sigma-Aldrich, USA) was added to freshly prepared 9 M HCl (Sigma-Aldrich, USA) aqueous solution. The mixture was stirred for 10 min to dissolve the salt, followed by the slow addition of 1 g $Ti_3AlC_2$ powder (Carbon, Ukraine; particle size: 40 μm). The mixture was maintained at 40 °C for 36 h. Thereafter, the resulting residue was washed repeatedly with DI water after centrifugation (10 min per cycle at 4000 rmp) until the pH of the supernatant reached approximately 6. The final product was filtered using a nylon filter and dried in air. Tetrapropyl ammonium hydroxide (TPAOH) treatment was used to further exfoliate the M-$Ti_3C_2T_x$ and produce N–$Ti_3C_2T_x$. Two grams of M-$Ti_3C_2T_x$ was immersed in TPAOH (25 wt% aqueous solution; Fisher-Scientific, USA) and stirred for three days at room temperature. Thereafter, the resulting residue was collected by cycles of centrifugation with water and ethanol and dried in air. A schematic illustration of the fabrication process for M-$Ti_3C_2T_x$ and N–$Ti_3C_2T_x$ is shown in Fig. 1a.

### 2.2. Synthesis of $TiO_2$-M-$Ti_3C_2T_x$ and $TiO_2$–N–$Ti_3C_2T_x$ hybrid photocatalysts

Anatase $TiO_2$ nanoparticles (100 nm) were first treated with 3-aminopropyl-trimethoxysilane (APTMS; Fisher-Scientific, USA), following the procedure reported by Lee et al. [28], to facilitate the interaction between $TiO_2$ and $Ti_3C_2T_x$. For synthesis of $TiO_2$-M-$Ti_3C_2T_x$ hybrids, two solutions were first prepared. Solution A: 40 mg of $TiO_2$ was dispersed in 40 mL distilled water by sonication for 50 min. Solution B: a specific weight percentage of M-$Ti_3C_2T_x$ (2.5, 5, 10, 15 or 30 wt% with respect to $TiO_2$) was dispersed in 10 mL distilled water by ultrasonication for 50 min. Then, solution B was added dropwise to solution A under stirring and the resulting mixture was stirred for 50 min. Thereafter, the $TiO_2$-M-$Ti_3C_2T_x$ hybrid was collected by centrifugation and dried in air. For synthesis of $TiO_2$–N–$Ti_3C_2T_x$, the same procedure was followed except M-$Ti_3C_2T_x$ was replaced with N–$Ti_3C_2T_x$. The schematic illustration of the fabrication process for $TiO_2$–N–$Ti_3C_2T_x$ is shown in Fig. 1b. For comparison, $TiO_2$–O–$Ti_3C_2T_x$ was also synthesized by calcination of 300 mg of M-$Ti_3C_2T_x$ in air at 450 °C for 4 h. $TiO_2$–N–$Ti_3C_2T_x$ and $TiO_2$-M-$Ti_3C_2T_x$ were synthesized following the process used in the synthesis of $TiO_2$–N–$Ti_3C_2T_x$ and $TiO_2$-M-$Ti_3C_2T_x$ but by using $TiO_2$ (Degussa P25).

### 2.3. Characterization

Images were acquired with a scanning electron microscope (SEM, Hitachi S4700 II cFEG) at an accelerating voltage of 10 kV using the secondary electron detector. Transmission electron microscopy (TEM) was conducted with a Thermo Fisher Scientific G2 Tecnai F30 FEG high-resolution microscope. SEM and TEM were used to characterize the morphologies of $Ti_3C_2T_x$ and the synthesized photocatalysts. For TEM, a small amount of the sample was dispersed in ethanol by sonication and drop cast on a copper microgrid coated with lacey carbon. The images were acquired at an accelerating voltage of 300 kV. Fourier transform infrared (FTIR) was exploited to detect the presence of functional groups on the surface of $Ti_3C_2T_x$ and the hybrid photocatalyst. FTIR spectra were recorded on a Cary 630 Agilent spectrometer at a resolution of 4 $cm^{-1}$. Raman spectroscopy was utilized to study the compositions and surface functional groups of $Ti_3C_2T_x$ and the hybrid photocatalysts. Raman spectra were obtained by Renishaw InVia Raman microscope with an excitation wavelength of 532 nm. X-ray photoelectron spectroscopy (XPS) was used to probe the surface chemistry of $Ti_3C_2T_x$ and the hybrid photocatalysts. XPS data were collected using a PHI 5000 VersaProbe II (Physical Electronics Inc.) system at ultrahigh vacuum ($1 \times 10^{-9}$ bar) with a monochromated Al $k_\alpha$ X-ray source. The charge compensation was achieved with a combination of electron and argon ion flood guns. The X-ray beam size was 100 μm and survey spectra were recorded with pass energy (PE) of 117 eV, step size of 1 eV and dwell time of 20 m s; whereas high-energy resolution spectra were recorded

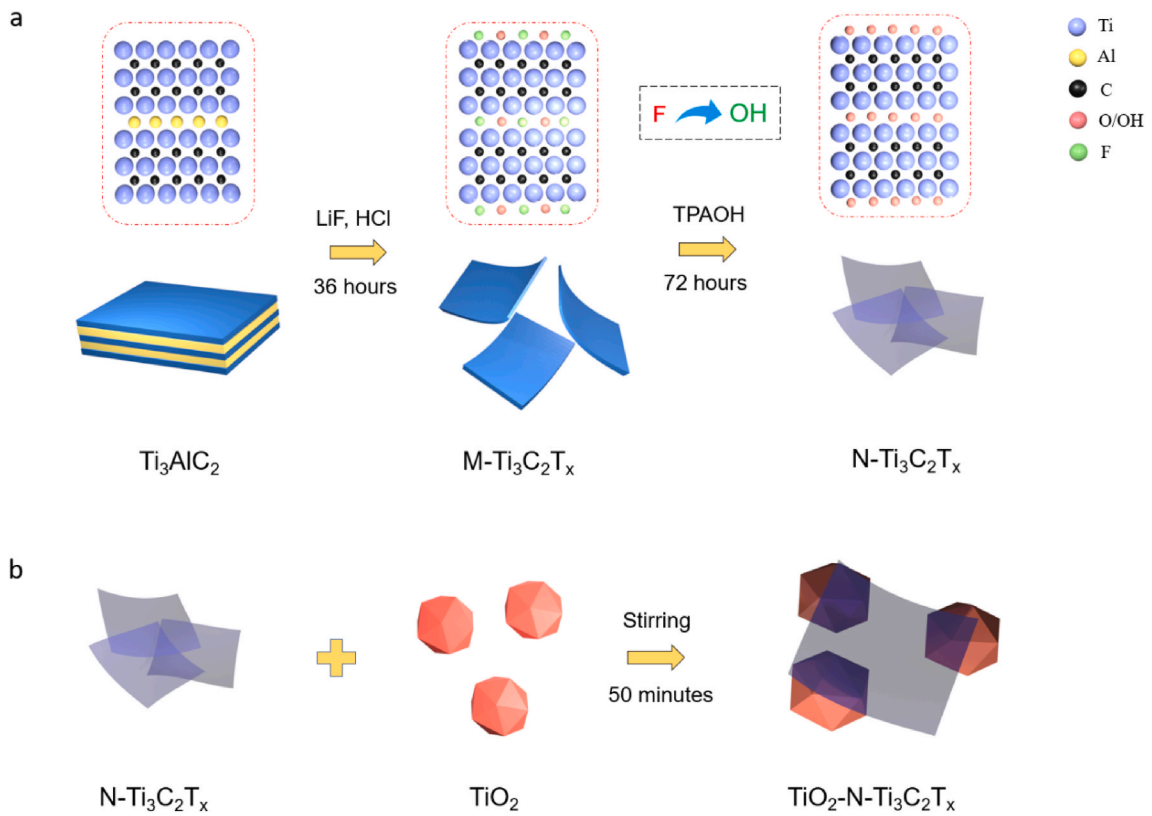


**Fig. 1.** Schematic illustrations of the synthesis steps of N–$Ti_3C_2T_x$ (a) and $TiO_2$–N–$Ti_3C_2T_x$ (b).

with PE of 47 eV, step size 0.1 eV and dwell time of 20 m s. Auto-z (i.e., automated height adjustment to the highest intensity) was performed before each measurement to find the analyzer's focal point. The number of average sweeps of each of the elements was adjusted (5–15 sweeps) to obtain the optimal signal-to-noise ratio. Raman and XPS data were fit to Gaussian curves by OriginPro® [29].

Optical properties of $Ti_3C_2T_x$ and the hybrid photocatalysts were studied using a variety of spectroscopic techniques. UV–Visible (UV–Vis) spectra were obtained using a Shimadzu UV-2600 spectrometer with $BaSO_4$ as the background material. Photoluminescence (PL) spectroscopy was utilized to investigate electron-hole recombination in the hybrid photocatalysts. PL spectra were acquired via a spectraMax i3x multi-mode microplate reader over the range of 400–700 nm using an excitation wavelength of 360 nm. Electron paramagnetic resonance (EPR) spectroscopy was employed to detect the generation of •OH radicals on the hybrid photocatalysts using 5,5-dimethyl-1-pyrroline N-oxide (DMPO, Enzo Life Sciences, Plymouth Meeting, MI, USA) as a spin trap. In brief, an aliquot (950 μL) of aqueous dispersion of the hybrid photocatalyst (1 mg in 5 mL water) was mixed with 50 μL aqueous solution of DMPO to a final spin probe concertation of 100 μM. The mixture was exposed to UV-light for 5 min to generate •OH radicals, then sampled into borosilicate EPR tubes (100 μL) for subsequent EPR analysis (SpinscanX, ADANI, Minsk, Belarus). The formation of DMPO spin adducts was quantified by calculating the total area under the curve via double-integration of the characteristic EPR peaks using GRAMS/AI™ Spectroscopy Software (Thermo Scientific™, Version 9).

### 2.4. Photocatalytic activity evaluation

#### 2.4.1. Liquid phase

Photocatalytic activity of $TiO_2$ and synthesized photocatalysts in liquid phase were evaluated by the degradation of MB in a batch reactor under UV light irradiation at room temperature and pH = 7. In a typical experiment, an aqueous solution of MB (8 mL of 0.04 mg/mL) was placed in the batch reactor, and 4 mg of photocatalyst was added under constant stirring. In the dark, the mixture was stirred for 30 min to achieve adsorption and desorption equilibrium between the photocatalyst and MB. Thereafter, the stirring was continued under UV illumination and a small amount of slurry was taken every 5 min and analyzed by UV–Vis spectroscopy. The illumination system consists of two 25 W UV lamps (Sylvania 21703) without reflectors and the main wavelength of the lamp is 356 nm. Prior to UV–Vis analysis, the photocatalyst was recovered by centrifugation; MB concentration was determined by recording the change in absorbance at 664 nm. Based on the experimental data, the photocatalytic degradation of MB was fitted to a pseudo first-order reaction:

$$\frac{c}{c_0} = e^{-kt}$$

where $k$ is the apparent constant of reaction rate, $c$ is the concentration of MB, and $t$ is the reaction time.

#### 2.4.2. Gas phase

Photocatalytic activity of $TiO_2$ and synthesized photocatalysts in gas phase was evaluated by the oxidation of $NO_x$ in a continuous flow reactor, described elsewhere [30,31]. A substrate coated with a photocatalyst was loaded into the reactor and irradiated with UV light for 1 h under continuous airflow to remove adsorbed contaminants. Then, the light was turned off and the $NO_x$ was introduced to the reactor for adequate adsorption of gaseous molecules on the photocatalyst surface. After 30 min, the light was turned on and the reaction was monitored at 1.0 ppm NOx with a total airflow of 3000 sccm at a relative humidity of 50%. After 2 h of reaction, the light was turned off and $NO_x$ was allowed to re-equilibrate. Average concentrations of NO, $NO_2$ and $NO_x$ were determined by averaging all data obtained during the oxidation reaction.

To compare the photocatalytic activity, $DeNO_x$ index, an objective figure of merit for photocatalytic $NO_x$ abatement, was utilized. DeNOx

index quantifies the net $NO_x$ removal by considering NO conversion and product selectivity, defined as the percentage of NO completely oxidized to nitrates versus the total amount of NO oxidized to $NO_2$. To calculate DeNOx index, the photonic efficiency for NO, $NO_2$ and $NO_x$ was first calculated using Equation (1) [32].

$$\xi = \frac{(c_d - c_i)\dot{V}p}{\varphi ART} \tag{1}$$

where $\xi$ is the photonic efficiency of a given specie; $c_d$ is the species concentrations in the dark; $c_i$ is the species concentrations under illumination; $\dot{V}$ is the volumetric flow rate; $p$ is the pressure in system (1 atm); $\varphi$ is the photon flux at the photocatalyst surface (dependent of light wavelength and intensity); $A$ is the catalyst irradiated area; $R$ is the gas constant; $T$ is the temperature.

The calculated photonic efficiencies were then used to calculate the $DeNO_x$ index and the selectivity by using Equations (2) and (3), respectively.

$$DeNO_x\ index = \xi_{NO_x}\left(3 - \frac{2}{S}\right) \tag{2}$$

$$S = \frac{\xi_{NO_x}}{\xi_{NO}} \tag{3}$$

## 3. Results and discussion

### 3.1. Characterization of M-$Ti_3C_2T_x$ and N–$Ti_3C_2T_x$

#### 3.1.1. Morphology

From the SEM image of $Ti_3AlC_2$ in Fig. 2a, the characteristic smooth surface of MAX phase is apparent. After etching the MAX phase with LiF and HCl, the resulting exfoliated M-$Ti_3C_2T_x$ (Fig. 2b) exhibits the typical morphology of MXene produced by the so called "minimally intensive layer exfoliation" process [33]. Subsequent treatment with TPAOH yielded highly exfoliated MXene flakes as verified by the SEM image in Fig. 2c, where the separated flakes can be easily observed. It is clear from the TEM images (Fig. 2d and e) that the flakes of N–$Ti_3C_2T_x$ are thinner and smaller than those of M-$Ti_3C_2T_x$. TEM-derived lateral dimensions of M-$Ti_3C_2T_x$ and N–$Ti_3C_2T_x$ were determined by averaging the length (longest distance) and width (shortest distance) of MXene sheets, following the approach reported by Xia et al. [34]. For both M-$Ti_3C_2T_x$ and N–$Ti_3C_2T_x$, lateral dimensions of 106 sheets were first determined and the dimensions obtained are shown using a histogram with a curve of the fitted log-normal distribution (Fig. 2g and h and Fig. S1). Our analysis reveals that the average lateral dimensions of M-$Ti_3C_2T_x$ and N–$Ti_3C_2T_x$ are 1.34 ± 0.5 μm and 181 ± 86 nm, respectively. The HR-TEM image of N–$Ti_3C_2T_x$ (Fig. 2f) confirms the sheets are ultrathin, and the corresponding fast Fourier transform (FFT) reveals a highly crystalline lattice of N–$Ti_3C_2T_x$ basal plane. UV–Vis spectra of M-$Ti_3C_2T_x$

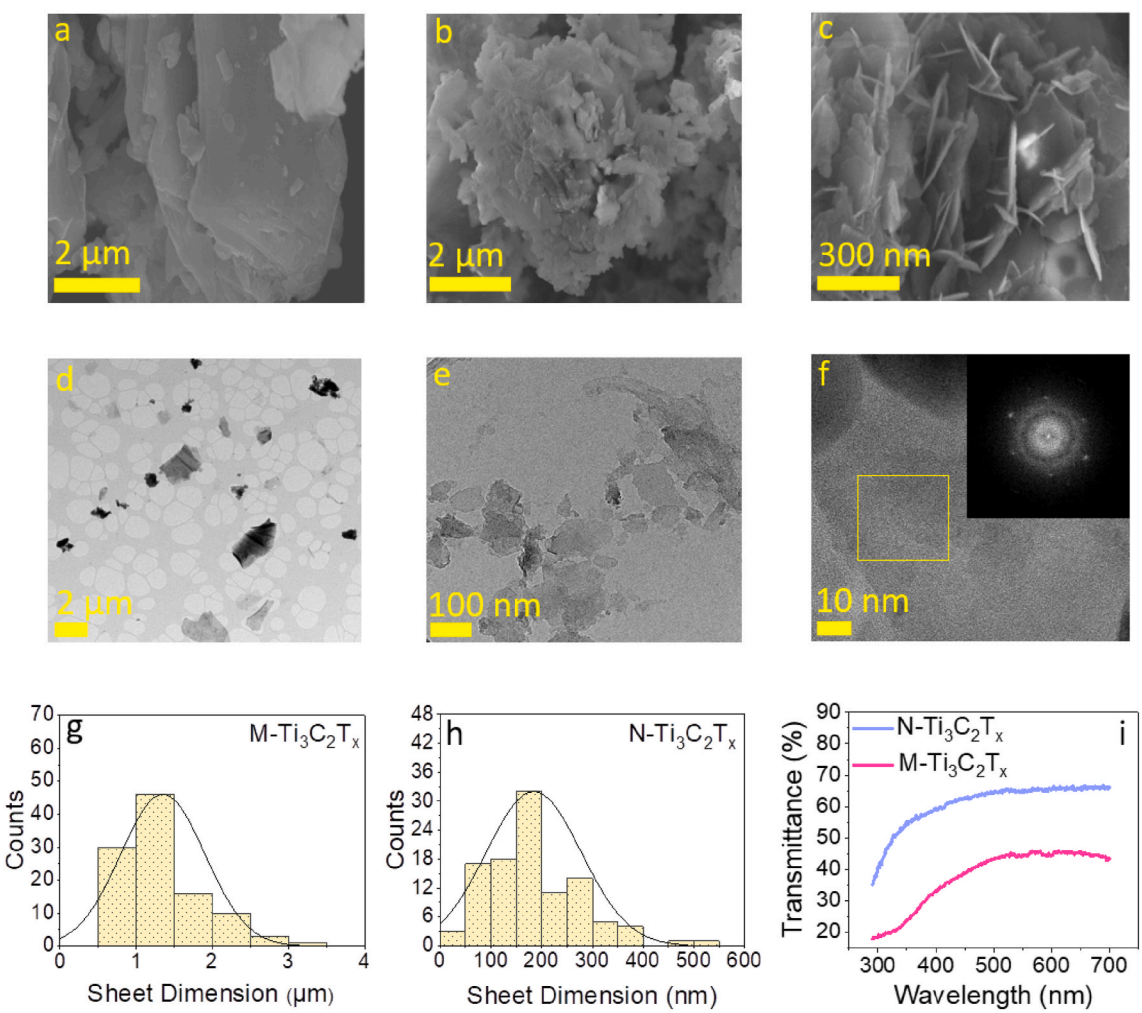


**Fig. 2.** SEM images of $Ti_3AlC_2$ (a), M-$Ti_3C_2T_x$ (b), and N–$Ti_3C_2T_x$ (c). TEM images of M-$Ti_3C_2T_x$ (d) and N–$Ti_3C_2T_x$ (e). HR-TEM image of N–$Ti_3C_2T_x$ (f) and the FFT pattern corresponding to the yellow square in f (inset). Dimension distribution histograms of M-$Ti_3C_2T_x$ (g) and N–$Ti_3C_2T_x$ (h) from TEM images. UV–Vis spectra of M-$Ti_3C_2T_x$ and N–$Ti_3C_2T_x$ dispersions in water (i).

and N–$Ti_3C_2T_x$ dispersions in water (Fig. 2i), reveal a transmittance of approximately 65% for N–$Ti_3C_2T_x$ and 40% for M-$Ti_3C_2T_x$, indicating N–$Ti_3C_2T_x$ is more transparent than M-$Ti_3C_2T_x$. The strong absorption peak below 300 nm is attributed to the optical glass cuvettes used in the measurement.

Further structural characterization of the MXenes was carried out using XRD and Raman spectroscopy. XRD spectra of $Ti_3AlC_2$, M-$Ti_3C_2T_x$, and N–$Ti_3C_2T_x$ are presented in Fig. 3a. The peaks at 2Θ = 9.5°, 19.2°, 34.0°, 36.8°, 39.0°, 41.8°, 44.9°, 48.5°, 52.4°, 56.5°, and 60.3° are indexed to the (002), (004), (101), (103), (104), (105), (106), (107), (108), (109), and (110) planes of $Ti_3AlC_2$, respectively [35,36]. The decrease in structural order and crystallinity are apparent after Al etching, as evidenced by the broadening of the diffraction peaks of M-$Ti_3C_2T_x$ and N–$Ti_3C_2T_x$. For M-$Ti_3C_2T_x$, the (002) peak broadens and shifts to lower angle (2Θ = 6.2°) due to the increase in *d*-spacing, which is a consequence of expansion of the lattice from Al removal and introduction of terminal functional groups. Interestingly, the shift in (002) peak is regarded as an indication of the successful exfoliation of MXene sheets [36]. In the case of N–$Ti_3C_2T_x$, the (002) peak also shifts to lower angle (2Θ = 5.5°), indicating a change in surface terminal groups and the formation of highly exfoliated sheets. In both M-$Ti_3C_2T_x$ and N–$Ti_3C_2T_x$, the peaks at 35.9 and 41.7 can also be ascribed to TiC impurities, most likely formed during the fabrication process of $Ti_3AlC_2$ [37]. Raman spectra of $Ti_3AlC_2$, M-$Ti_3C_2T_x$, and N–$Ti_3C_2T_x$ are shown in Fig. 3b. The decrease in the intensities of peaks in the region between 200 and 700 $cm^{-1}$ for M-$Ti_3C_2T_x$ and N–$Ti_3C_2T_x$ after Al etching is due to their structural deterioration and loss of crystallinity, which is consistent with the XRD results [1,36,38]. The phenomenon is accompanied by broadening of Raman peaks corresponding to the D-band (~1319 $cm^{-1}$) and G-band (~1596 $cm^{-1}$); these features are usually apparent after exfoliation of MXenes and generation of graphitic carbon and defects [39,40].

### 3.1.2. Chemical properties

It has been shown that the lattice vibration of $Ti_3C_2T_x$ is very sensitive to the type of terminal functional groups attached to the surface [41,42]. Raman spectroscopy is therefore a powerful tool for investigating the surface chemistry of $Ti_3C_2T_x$. In this regard, the Raman spectra of M-$Ti_3C_2T_x$ and N–$Ti_3C_2T_x$ were deconvoluted into three regions as shown in Fig. 3c and d. The three regions in M-$Ti_3C_2T_x$ (Fig. 3c) are classified as the flake region, functional terminal region, and carbon region. First, the flake region between 100 and 210 $cm^{-1}$ corresponds to a group vibration of carbon and two Ti layers. In this region, the two peaks at 154 and 190 $cm^{-1}$ represent the in-plane vibrations of surface Ti2 and C atoms in $Ti_3C_2$ and the out-of-plane vibration of Ti2 and C atoms in $Ti_3C_2F_2$, respectively [39,43,44]. Second, the functional terminal region between 210 and 500 $cm^{-1}$ corresponds to the vibrations of surface groups. In this region, the peaks at 251, 399 and 430 $cm^{-1}$ are assigned to the in-plane vibrations of surface groups attached to Ti atoms in $Ti_3C_2O(OH)$, $Ti_3C_2(OH)_2$ and $Ti_3C_2O(OH)$, respectively [42]. Third, the carbon region between 500 and 800 $cm^{-1}$ corresponds to in-plane and out-of-plane C atom vibrations. The peaks at 599 and 709

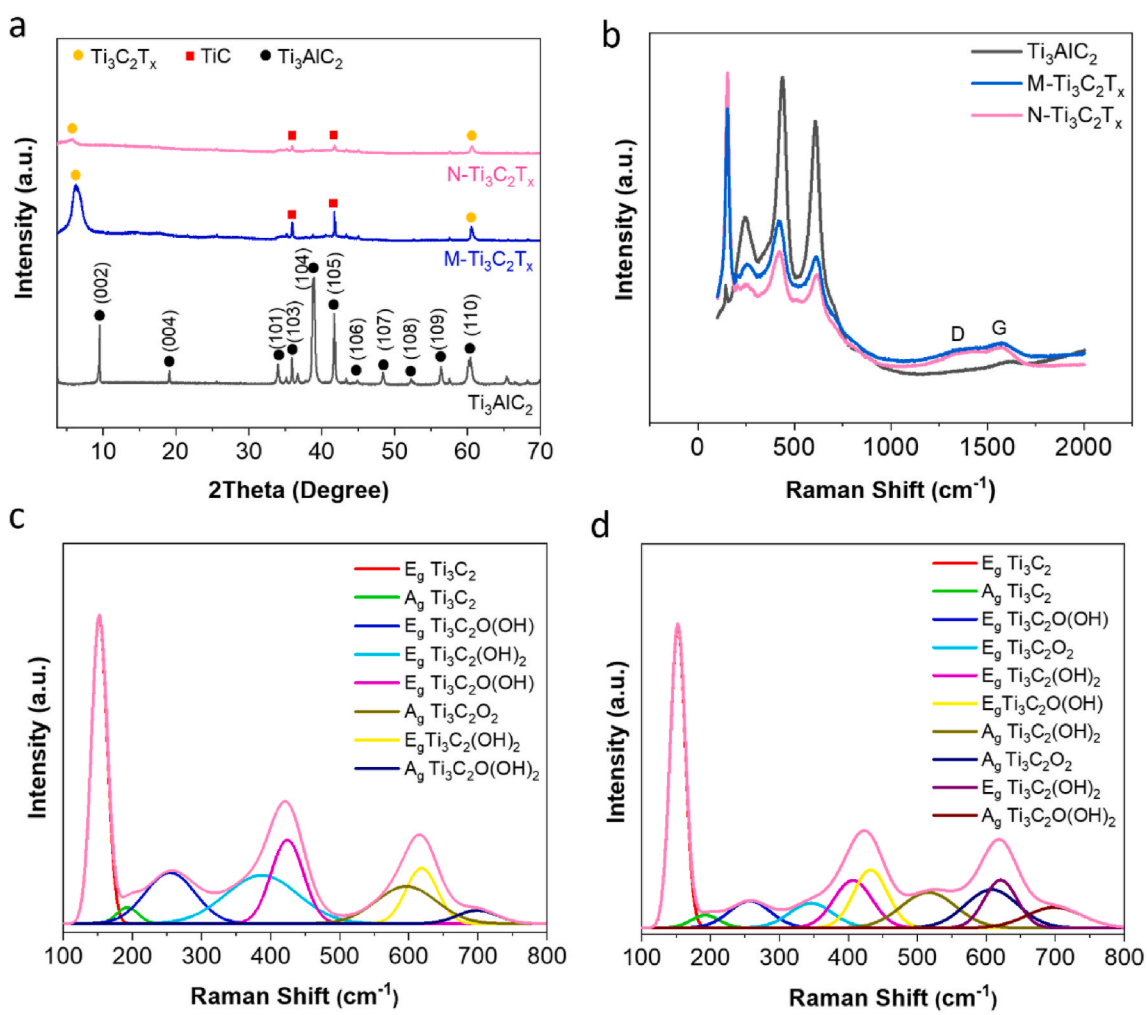


**Fig. 3.** XRD spectra of $Ti_3AlC_2$, M-$Ti_3C_2T_x$ and N–$Ti_3C_2T_x$ (a). Raman spectra of $Ti_3AlC_2$, M-$Ti_3C_2T_x$ and N–$Ti_3C_2T_x$ (b). Deconvoluted Raman spectra of M-$Ti_3C_2T_x$ (c) and N–$Ti_3C_2T_x$ (d).

$cm^{-1}$ are attributed to out-of-plane vibration of C atoms in $Ti_3C_2O_2$ and $Ti_3C_2O(OH)_2$, respectively [42], whereas the peak at 622 $cm^{-1}$ is assigned to the in-plane vibration of C atoms in $Ti_3C_2(OH)_2$ [39,45]. In the case of N–$Ti_3C_2T_x$ (Fig. 3d), the appearance of peaks at 347 $cm^{-1}$ in the functional terminal region (corresponding to the in-plane vibration of functional groups in $Ti_3C_2O_2$) and 514 $cm^{-1}$ in the carbon region (corresponding to the out-of-plane vibration of C atoms in $Ti_3C_2(OH)_2$) reveals the change in surface groups upon treating the M-$Ti_3C_2T_x$ with TPAOH [42,44]. The change in the terminal functional groups of M-$Ti_3C_2T_x$ upon TPAOH treatment was corroborated by FTIR analysis, evidenced by peaks corresponding to C–O, C═O, OH and COOH exhibiting substantially higher intensities in N–$Ti_3C_2T_x$ than M-$Ti_3C_2T_x$ (Fig. S2).

To further investigate the surface chemistry of $Ti_3C_2T_x$, high-resolution XPS of Ti 2p, O 1s and C 1s core levels were conducted for M-$Ti_3C_2T_x$ and N–$Ti_3C_2T_x$ and the results are shown in Fig. 4. For M-$Ti_3C_2T_x$, the Ti $2p_{3/2}$ ($2p_{1/2}$) spectrum (Fig. 4a) was deconvoluted into six peaks, corresponding to Ti–C, Ti(II), Ti(III), Ti(IV), $TiO_{2-x}F_x$ and Ti–F. The peak at 454.4 (460.6) eV is assigned to Ti–C and originates from the interior Ti atoms in M-$Ti_3C_2T_x$ [18,46,47]. The peaks at 455.7 (461.8), 457.7 (463.3) and 458.8 (464.5) eV correspond to Ti oxidation states and can be attributed to OH/O–$Ti^{2+}$-C, OH/O–$Ti^{3+}$-C and $TiO_2$, respectively [46,47]. The peaks at 459.5 (465.2) and 460.5 (466.5) eV are assigned to $TiO_{2-x}F_x$ and C–Ti–F [48]. The O 1s spectrum was deconvoluted into five peaks (Fig. 4b) at 529.7, 530, 530.6, 531.8 and 533.1 eV and assigned to $TiO_2$, $TiO_{2-x}F_x$, C–Ti-$O_x$, C–Ti-$(OH)_x$ and $H_2O_{ads}$, respectively [20,46,48]. The deconvolution of C 1s spectrum produces seven peaks (Fig. 4c) at 281 and 282.2, 284, 284.7, 285, 286 and 288.7 eV and are attributed to C–Ti-$T_x$, C═C, C–C, C–H, C–O and COO, respectively [46,48–52]. XPS peak fitting shows the dominant terminals on M-$Ti_3C_2T_x$ surface are = O, –OH and –F, consistent with the Raman analysis.

For N–$Ti_3C_2T_x$, the binding energies of Ti peaks are shifted to lower values (Fig. 4d), most likely due to the introduction of defects as a result of TPAOH treatment—a phenomenon that has been observed in transition metal carbides [48]. The Ti–C, (OH or O)–$Ti^{2+}$-C, (OH or O)–$Ti^{3+}$-C, $TiO_2$ and C–Ti-$F_x$ are located at 453.8 (459.5), 455.8 (461.5), 457.0 (462.7), 457.6 (463.5) and 458.4 (464.4) eV [39,48,53]. The peaks corresponding to $TiO_2$ (528.9 eV), C–Ti-$O_x$ (531.4 eV) and C–Ti-$(OH)_x$ (530.4 eV) in O 1s region are preserved (Fig. 4e) [39,46]. In C 1s region (Fig. 4f), the peaks corresponding to C–Ti, C–Ti-$T_x$, C═C, C–C, and C–O are located at 280.3, 282.7, 284, 285 and 286.7 eV, respectively. In comparison to M-$Ti_3C_2T_x$, the intensity of peaks corresponding to $sp^2$ C and $sp^3$ C in N–$Ti_3C_2T_x$ is higher, indicating an increase in the amounts of graphitic carbon and defects in N–$Ti_3C_2T_x$ as observed in the Raman results. In contrast to M-$Ti_3C_2T_x$, no peak corresponding to $TiO_{2-x}F_x$ is observed in the Ti 2p and C 1s of N–$Ti_3C_2T_x$. We therefore conclude that TPAOH treatment reduces the amount of fluorine on the surface of $Ti_3C_2T_x$. Besides, the high-resolution XPS spectra in F 1s region show the decrease in the intensity of $F_x$ peak for N–$Ti_3C_2T_x$ in comparison to that of M-$Ti_3C_2T_x$ (Fig. S3). This observation, corroborated by FTIR and Raman analysis, indicates the N–$Ti_3C_2T_x$ is mainly terminated by = O and –OH functional groups. It is worth mentioning that the adsorption of pollutants such as MB, $CO_2$ and thiophene on $Ti_3C_2T_x$ surface is primarily controlled by –O and –OH functional groups [4,21–23]. Hence, the role of TPAOH is not only beneficial in altering the morphology of MXene, but also in adapting the surface chemistry for enhanced pollutant adsorption.

### 3.2. Characterization of $TiO_2$–N–$Ti_3C_2T_x$ and $TiO_2$-M-$Ti_3C_2T_x$ photocatalysts

TEM was utilized to investigate the morphology and interfacial contact between $Ti_3C_2T_x$ and $TiO_2$ in $TiO_2$-M-$Ti_3C_2T_x$ and $TiO_2$–N–$Ti_3C_2T_x$ hybrid photocatalysts. Fig. 5a and b reveal the highly exfoliated and transparent N–$Ti_3C_2T_x$ is in direct contact with $TiO_2$

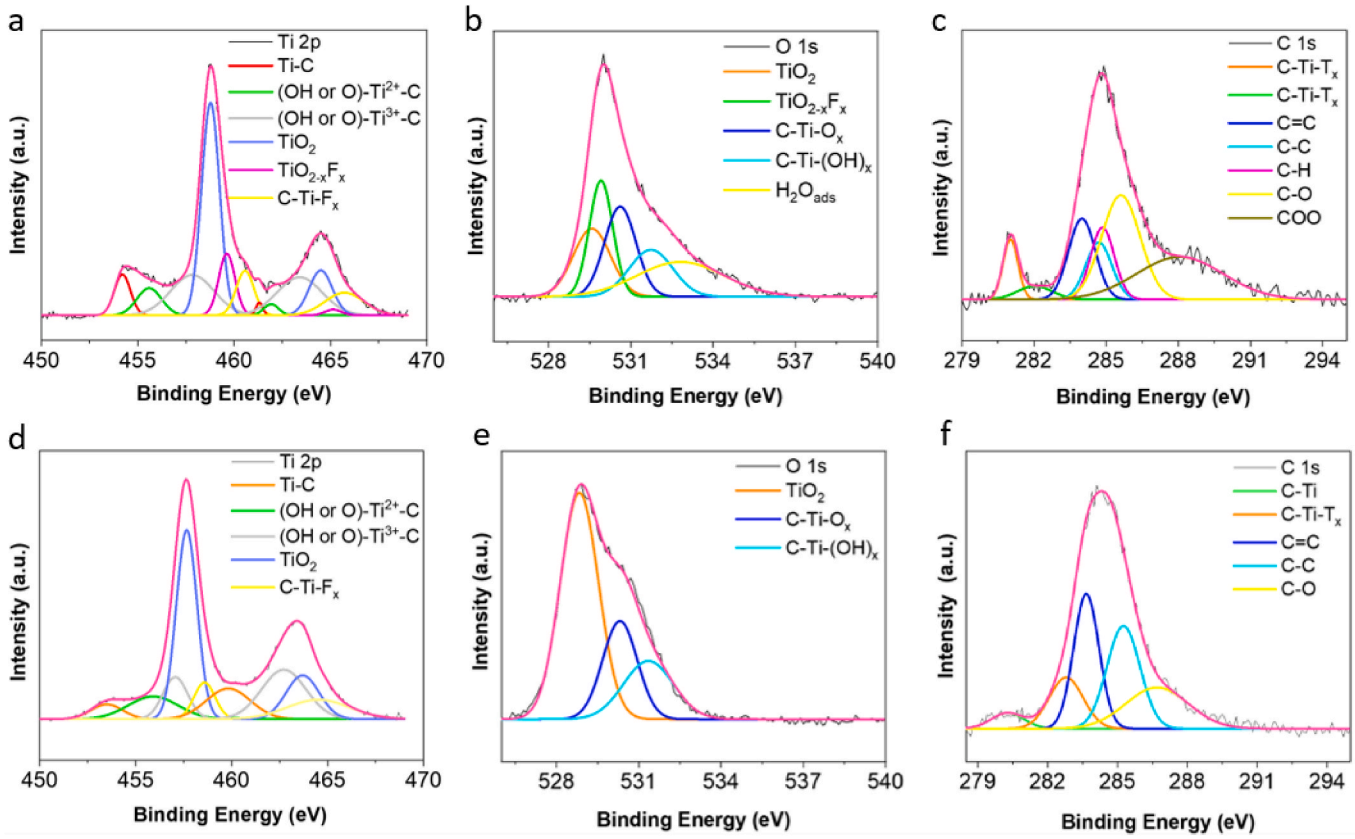


**Fig. 4.** High-resolution XPS spectra of M-$Ti_3C_2T_x$ in (a) Ti 2p, (b) O 1s and (c) C 1s. High-resolution spectra of N–$Ti_3C_2T_x$ in (d) Ti 2p, (e) O 1s and (f) C 1s.

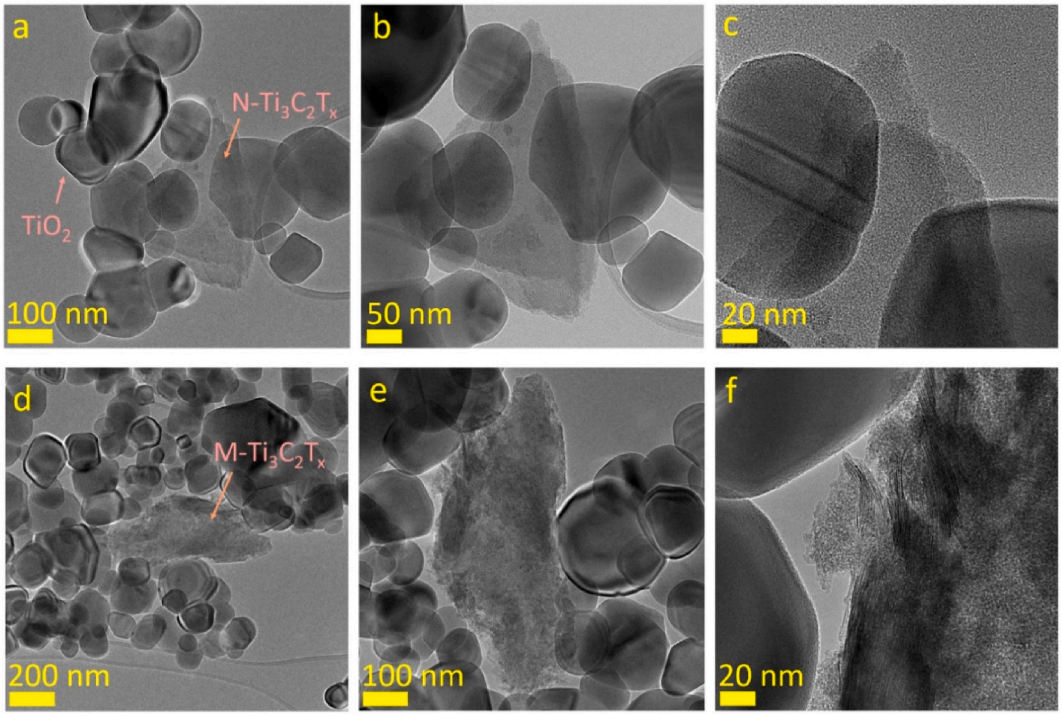


**Fig. 5.** TEM images of $TiO_2$–N–$Ti_3C_2T_x$ at different magnifications (a, b and c). TEM images of $TiO_2$-M-$Ti_3C_2T_x$ at different magnifications (d, e and f).

nanoparticles, and the high-magnification image (Fig. 5c) reveals the intimate interaction between N–$Ti_3C_2T_x$ and $TiO_2$ nanoparticles. The strong interfacial contact between N–$Ti_3C_2T_x$ and $TiO_2$ undoubtedly improves the quality of the junction formed between them, and is expected to facilitate charge carrier mobility across the interface. On the other hand, even though M-$Ti_3C_2T_x$ is exfoliated, the sample is thicker than N–$Ti_3C_2T_x$, and the $TiO_2$ nanoparticles tend to aggregate on the edges of M-$Ti_3C_2T_x$ (Fig. 5d and e). In addition, the high-magnification image in Fig. 5f shows the poor interfacial contact between $TiO_2$ nanoparticles and M-$Ti_3C_2T_x$ — in fact, only a small fraction of the nanoparticles is in direct contact with M-$Ti_3C_2T_x$ due to the low-quality junctions formed between the two components. The charge carrier mobility across the interface in $TiO_2$-M-$Ti_3C_2T_x$ is therefore diminished in comparison to $TiO_2$–N–$Ti_3C_2T_x$.

XRD spectra of $TiO_2$–N–$Ti_3C_2T_x$ and $TiO_2$-M-$Ti_3C_2T_x$ photocatalysts are shown in Fig. S4 a and b, where the peaks ascribed to anatase $TiO_2$ are obvious and consistent with the literature [54,55]. For $TiO_2$–N–$Ti_3C_2T_x$, the (002) peak of $Ti_3C_2T_x$ was not detected at low concentration of N–$Ti_3C_2T_x$, an observation that is consistent with our previous study whereby low amounts of SWCNTs were coupled with $TiO_2$ to facilitate electron-hole separation [56]. However, the peak intensity increases with concentration of N–$Ti_3C_2T_x$. A similar trend was observed for $TiO_2$-M-$Ti_3C_2T_x$, whereby the (002) peak of $Ti_3C_2T_x$ becomes dominant at high concentration of M-$Ti_3C_2T_x$. No peak associated with $Ti_3AlC_2$ was detected in both photocatalysts and the position of (002) peak for N–$Ti_3C_2T_x$ is still located at a lower angle than that of M-$Ti_3C_2T_x$ as observed in Fig. 3a, an indication that the highly exfoliated $Ti_3C_2T_x$ did not restack after coupling with $TiO_2$.

The Raman spectra of the pristine $TiO_2$ and $TiO_2$ modified with different concentrations of N–$Ti_3C_2T_x$ and M-$Ti_3C_2T_x$ are shown in Figs. S4c and d. The Raman spectra reveal the four characteristic peaks attributed to anatase vibration modes of $TiO_2$ [57,58]. Because the amount of N–$Ti_3C_2T_x$ and M-$Ti_3C_2T_x$ in the hybrids is small compared to that of $TiO_2$, no peak corresponding to $Ti_3C_2T_x$ is observed in the spectra of $TiO_2$–N–$Ti_3C_2T_x$ and $TiO_2$-M-$Ti_3C_2T_x$. However, at high concentrations of N–$Ti_3C_2T_x$ and M-$Ti_3C_2T_x$, the intensities of these dominant anatase vibrational modes dramatically decreased, indicating the existence of $Ti_3C_2T_x$ in the photocatalysts. To analyze the chemical composition of $TiO_2$–N–$Ti_3C_2T_x$ and $TiO_2$-M-$Ti_3C_2T_x$, XPS analysis was conducted and the results are summarized in Fig. S5. Because Ti and O coexist in both $Ti_3C_2T_x$ and $TiO_2$ and to avoid the possible overlap of the distinct peaks of $TiO_2$ and $Ti_3C_2T_x$ in Ti 2p and O 1s regions, our surface analysis of the compounds focuses on the high-resolution C 1s spectrum because carbon does not naturally exist in both compounds. The C 1s spectrum for $TiO_2$–N–$Ti_3C_2T_x$ was deconvoluted into six peaks (Fig. S5a) at 281, 283.2, 284, 284.6, 285.8 and 288 eV and attributed to T-C, Ti–C–O, C═C, C–C, CO and COO, respectively. On the other hand, the C 1s spectrum of $TiO_2$-M-$Ti_3C_2T_x$ (Fig. S5b) reveals peaks associated with Ti–O–C, C═C. C–C, CO and COO and located at 283.6, 284.3, 285.1, 286.4 and 288 eV, respectively [50,59], further confirming the existence of $Ti_3C_2T_x$ in the photocatalysts.

### 3.3. *Photocatalytic activity of $TiO_2$–N–$Ti_3C_2T_x$ and $TiO_2$-M-$Ti_3C_2T_x$ in liquid phase*

The photocatalytic activity of $TiO_2$–N–$Ti_3C_2T_x$ and $TiO_2$-M-$Ti_3C_2T_x$ in the degradation of MB (Fig. 6a, b and c) is sensitive to the amount of $Ti_3C_2T_x$ in the hybrid photocatalysts. Significant improvement in the photocatalytic activity of $TiO_2$ was achieved when the amounts of N–$Ti_3C_2T_x$ and M-$Ti_3C_2T_x$ in the hybrids were 30 wt% and 2.5 wt%, respectively; these compositions were considered as the optimum for the respective photocatalysts. The rate constant ($k$) for MB degradation using the optimized $TiO_2$–N–$Ti_3C_2T_x$ photocatalyst with 30 wt% N–$Ti_3C_2T_x$ is 0.046 $min^{-1}$, which is over three times higher than that of $TiO_2$ (0.013 $min^{-1}$), and two times higher than that of optimized $TiO_2$-M-$Ti_3C_2T_x$ with 2.5 wt% M-$Ti_3C_2T_x$ (0.023 $min^{-1}$). Self-photosensitization of MB under UV light is not considered as MB removal in the absence of a photocatalyst was negligible (data not shown for the sake of brevity). Interestingly, $TiO_2$–N–$Ti_3C_2T_x$ shows extremely high photocatalytic activity when compared to $TiO_2$–O–$Ti_3C_2T_x$ as shown in Fig. 7a and b. The nucleation of $TiO_2$ nanoparticles on $Ti_3C_2T_x$ surface and subsequent generation of $TiO_2$–O–$Ti_3C_2T_x$ by thermal oxidation was confirmed by TEM, FT-IR and PL analysis as shown in Fig. S6. The rate constant obtained for reaction

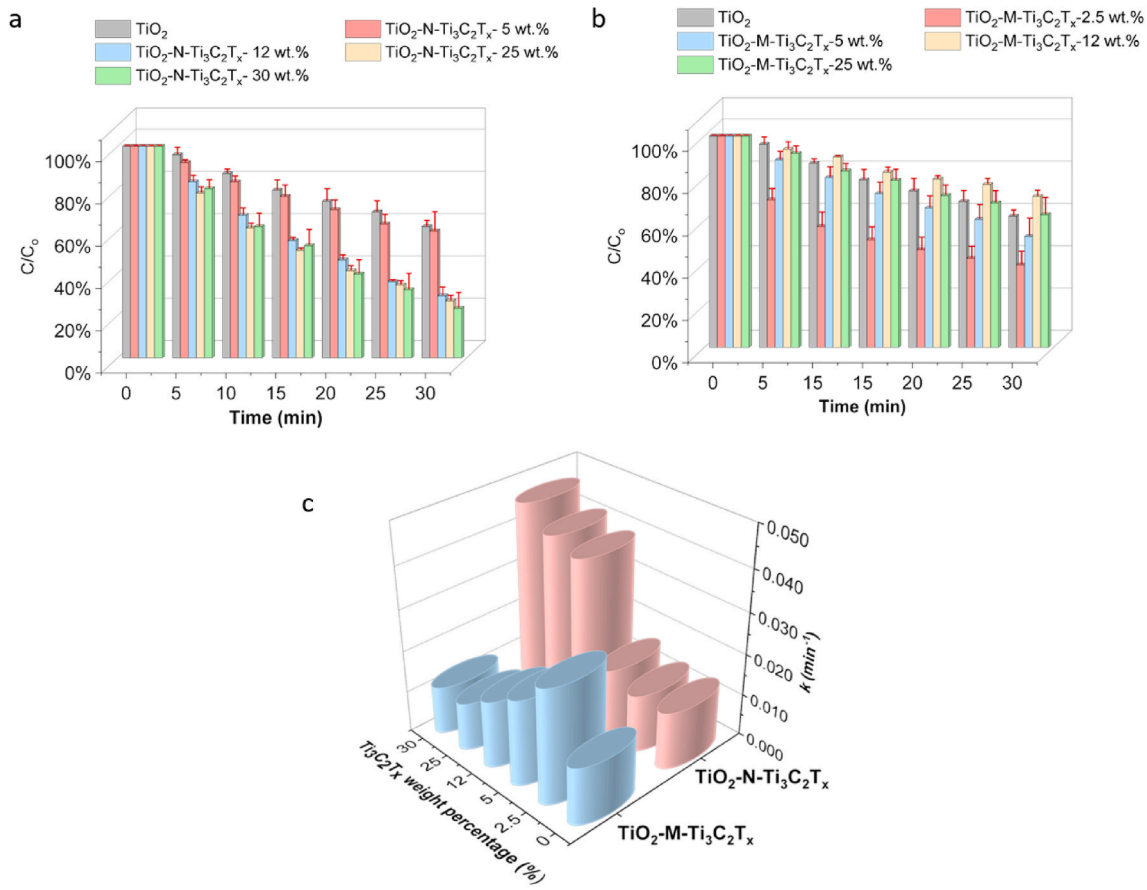


**Fig. 6.** Photocatalytic degradation of MB using $TiO_2$–N–$Ti_3C_2T_x$ (a) and $TiO_2$-M-$Ti_3C_2T_x$ (b) as a function of the amount of $Ti_3C_2T_x$ in the hybrids. Rate constant for MB photodegradation using $TiO_2$–N–$Ti_3C_2T_x$ and $TiO_2$-M-$Ti_3C_2T_x$ as a function of amount of $Ti_3C_2T_x$ (c). $TiO_2$ coupled with 2.5 wt% N–$Ti_3C_2T_x$ and 30 wt% M-$Ti_3C_2T_x$ are not included in (a) and (b) as their performance is similar to pristine $TiO_2$.

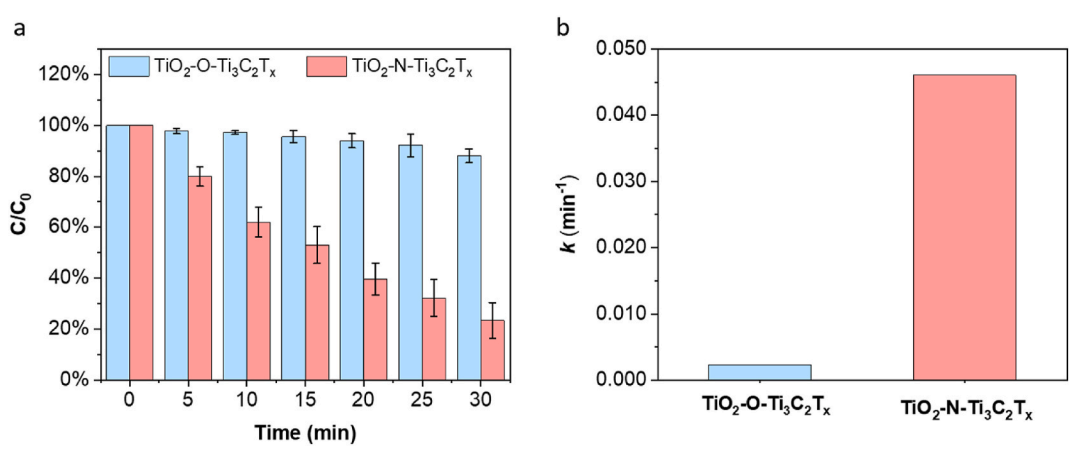


**Fig. 7.** Photocatalytic degradation of MB using $TiO_2$–O–$Ti_3C_2T_x$ and $TiO_2$–N–$Ti_3C_2T_x$ (a). Rate constant for MB photodegradation by $TiO_2$–O–$Ti_3C_2T_x$ and $TiO_2$–N–$Ti_3C_2T_x$ (b).

over $TiO_2$–N–$Ti_3C_2T_x$ is 20 times higher than that of $TiO_2$–O–$Ti_3C_2T_x$ ($k = 0.002\ min^{-1}$). Furthermore, $TiO_2$–N–$Ti_3C_2T_x$ exhibited good stability in four consecutive MB degradation experiments (Fig. S7).

Direct comparison of the activity of $TiO_2$–N–$Ti_3C_2T_x$ with other state-of-the-art photocatalysts in the literature can be misleading without a good understanding of the photocatalytic reaction conditions. Therefore, for meaningful comparison with our work, photocatalyst concentration, light wavelength, MB concentration and MB removal percentage from recent seminal studies are summarized in Table S1. It is clear that $TiO_2$–N–$Ti_3C_2T_x$ exhibits superior performance to other state-of-the-art photocatalysts especially at relatively low catalyst amount.

To rationalize the superior photocatalytic performance of $TiO_2$–N–$Ti_3C_2T_x$, we probed the PL emissions of $TiO_2$, $TiO_2$-M-$Ti_3C_2T_x$ and $TiO_2$–N–$Ti_3C_2T_x$. Fig. 8a shows the quenching in PL intensity after the addition of $Ti_3C_2T_x$, in which $TiO_2$–N–$Ti_3C_2T_x$ shows the lowest intensity. Since PL emissions are generated from free carrier recombination, a lower PL intensity indicates higher electron-hole separation [60]. The PL intensities reveal decreased electron-hole recombination was

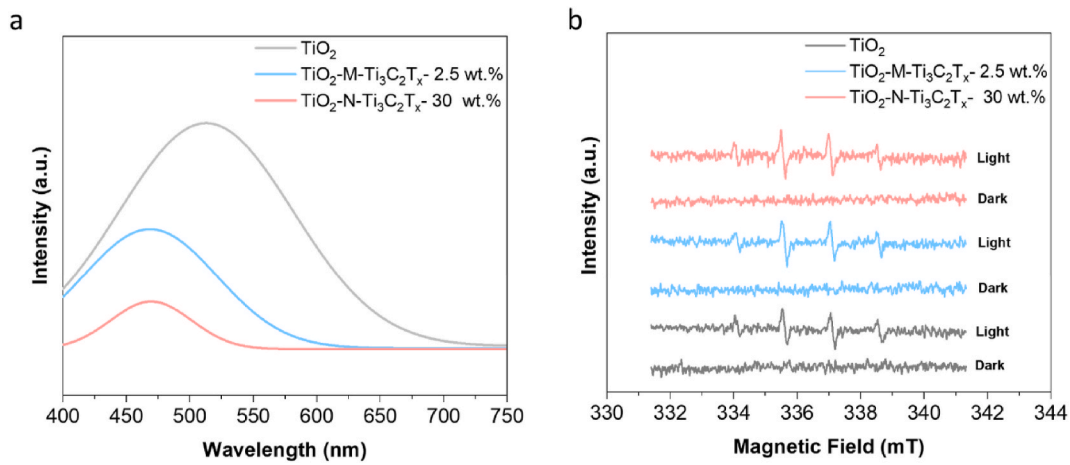


**Fig. 8.** PL spectra of $TiO_2$, $TiO_2$-M-$Ti_3C_2T_x$, and $TiO_2$–N–$Ti_3C_2T_x$ (a); and EPR spectra of DMPO-hydroxyl radical spin adducts produced from $TiO_2$, $TiO_2$-M-$Ti_3C_2T_x$, and $TiO_2$–N–$Ti_3C_2T_x$ in aqueous dispersion (0.2 mg/mL) after 5 min of UV irradiation (b).

achieved in $TiO_2$ that is coupled with N–$Ti_3C_2T_x$, which we attribute to the intimate interfacial contact between them, as verified earlier by TEM (Fig. 5c). The generation of •OH radicals on the catalyst surface, a key step in the photocatalytic degradation process, is generally attributed to the interaction between photogenerated holes and water molecules [61]. This claim is supported by our results in Fig. S8 that show poor MB degradation by $TiO_2$–N–$Ti_3C_2T_x$ in the presence of a hole scavenger (ethanol). To investigate the generation of •OH radicals on $TiO_2$ and the hybrid photocatalysts, EPR with a DMPO spin trap approach was utilized. As shown in Fig. 8b, the peaks detected in EPR spectra of $TiO_2$, $TiO_2$-M-$Ti_3C_2T_x$ and $TiO_2$–N–$Ti_3C_2T_x$ were negligible before light exposure.

Contrarily, after 5 min of light irradiation, the three photocatalysts show noticeable peaks which are attributed to the photogeneration of •OH radicals [2,62]. The intensity of EPR peaks detected in the presence of $TiO_2$–N–$Ti_3C_2T_x$ was greater than that of pristine $TiO_2$ and $TiO_2$-M--$Ti_3C_2T_x$; the areas under the characteristic DMPO quadruplet spectra of $TiO_2$, $TiO_2$-M-$Ti_3C_2T_x$, and $TiO_2$–N–$Ti_3C_2T_x$ were 230, 243.5, and 260 (a.u.), respectively. Based on EPR theory, the areas calculated via double-integration are proportional to the number of spin adducts formed by •OH radicals and DMPO integrated [63], and therefore, higher values indicate higher concentration of •OH radicals on catalyst surface. The EPR analysis further confirms the effective electron-hole separation in $TiO_2$–N–$Ti_3C_2T_x$ and subsequent generation of •OH radicals on the surface. As shown earlier, the UV–Vis data reveal the high transparency of N–$Ti_3C_2T_x$, indicating its presence in the hybrid structure does not hinder light penetration to $TiO_2$, which ensures excellent photon-$TiO_2$ interactions during photocatalytic reaction, as opposed to the thick M-$Ti_3C_2T_x$ with relatively lower transparency.

Furthermore, it has been shown that the positively charged MB molecules can be easily adsorbed on negatively charged terminals (particularly, on oxygen-containing terminals) of $Ti_3C_2T_x$, leading to their subsequent removal from water [21,22]. Hence, it is reasonable to hypothesize that the abundant oxygen-containing terminals on N–$Ti_3C_2T_x$ are also contributing to the superior degradation of MB achieved by $TiO_2$–N–$Ti_3C_2T_x$. To test the hypothesis, we reduced the number of sites available for MB adsorption through sodium ion-intercalation. It has been shown that upon dispersion of $Ti_3C_2T_x$ in NaOH aqueous solution, the negatively charged groups on the surface are compensated by $Na^+$ [64]. The attachment to the negatively charged functional groups, which occurs most likely via ionic bonds, should reduce the available sites for MB adsorption and as a result hamper the non-photocatalytic route for MB removal. N–$Ti_3C_2T_x$ with $Na^+$, designated as Na–$Ti_3C_2T_x$ was obtained after treatment with NaOH. The presence of $Na^+$ on MXene surface was confirmed by XPS as shown in the high-resolution scan in Fig. S9, where a peak at 1072 eV, attributed to $Na^+$, is detected [65]. Na–$Ti_3C_2T_x$ was then coupled with $TiO_2$ to produce a hybrid structure (designated as $TiO_2$-Na–$Ti_3C_2T_x$), which was also used in photocatalytic removal of MB. Results in Fig. 9a and b show MB removal by $TiO_2$–Na–$Ti_3C_2T_x$ is lower than that achieved by $TiO_2$–N–$Ti_3C_2T_x$. The reduction in catalyst activity upon using Na–$Ti_3C_2T_x$ as a cocatalyst instead of N–$Ti_3C_2T_x$ is attributed to the decrease of sites available for MB adsorption and subsequent decrease in the removal rate of MB by the non-photocatalytic route. It is important to highlight the following: (1) treating MXene with NaOH does not compromise its ability to separate the photogenerated charges [4]; (2) although adsorption of MB on Na–$Ti_3C_2T_x$ can still occur via ion exchange between MB and $Na^+$, previous investigations showed that the attachment of adsorbates on functional terminals of MXene is dominated by electrostatic attraction and hydrogen bonds [21,22,66]. We therefore conclude that the high photon-$TiO_2$ interaction and MB adsorption, as well as the reduced electron-hole recombination are responsible for the superior photocatalytic activity of $TiO_2$–N–$Ti_3C_2T_x$.

For liquid-phase reactions, pH of solution is an important factor that should be considered as it impacts both the surface charge of photocatalysts and the generation of •OH radicals. Hence, we conducted the degradation of MB in acidic and basic solutions using $TiO_2$–N–$Ti_3C_2T_x$ photocatalyst (Fig. 10a and b). In basic solution (pH = 11), the photocatalytic activity is significantly lower than that achieved at neutral environment (pH = 7). In the basic solution, the generation of •OH radicals is suppressed due to deprotonation of photocatalytic reaction intermediate on $TiO_2$ [67], and hence, the degradation rate of MB decreases. In addition, it has been suggested that increasing the basicity of the solution (i.e. pH > 8) favors electron-hole recombination on catalyst surface [68], which could be another reason for the observed reduction in the photocatalytic activity. In contrast, at pH = 2, the photocatalytic removal rate of MB decreased slightly compared to that at pH = 7. Since previous investigations imply that increasing the acidity of solution has no influence on the generation of ROS [68,69], this slight reduction in photocatalytic activity is attributed to the reduction in MB adsorption on N–$Ti_3C_2T_x$. In acidic solution, the negative zeta potential of N–$Ti_3C_2T_x$ decreases, and in turn, decreases the electrostatic attraction between the cationic MB and N–$Ti_3C_2T_x$ surface [70], inhibiting the adsorption of MB on the catalyst surface and subsequent MB removal via the non-photocatalytic route.

### *3.4. Photocatalytic activity of $TiO_2$–N–$Ti_3C_2T_x$ and $TiO_2$-M-$Ti_3C_2T_x$ in gas phase*

To demonstrate the versatility of N–$Ti_3C_2T_x$ as a cocatalyst in

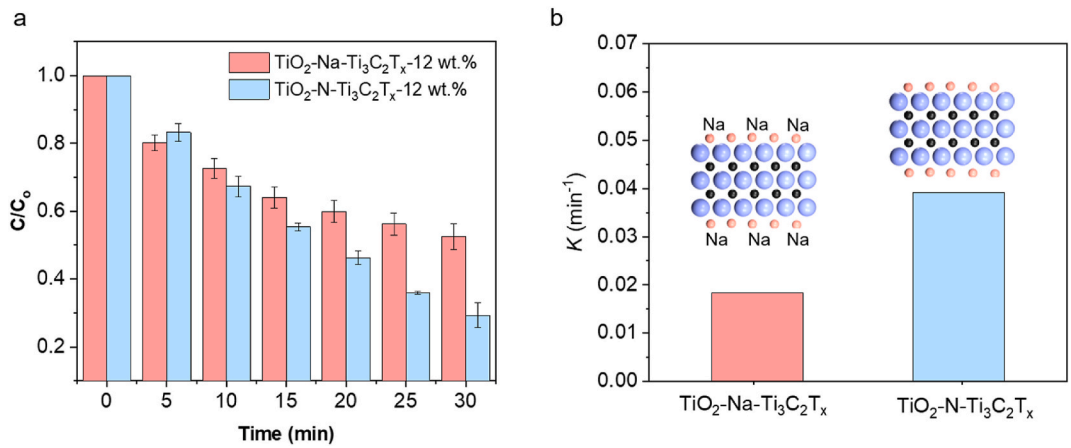


**Fig. 9.** Photocatalytic degradation of MB using $TiO_2$–Na–$Ti_3C_2T_x$ and $TiO_2$–N–$Ti_3C_2T_x$ (a). Rate constant for MB photodegradation by $TiO_2$–Na–$Ti_3C_2T_x$ and $TiO_2$–N–$Ti_3C_2T_x$ (b).

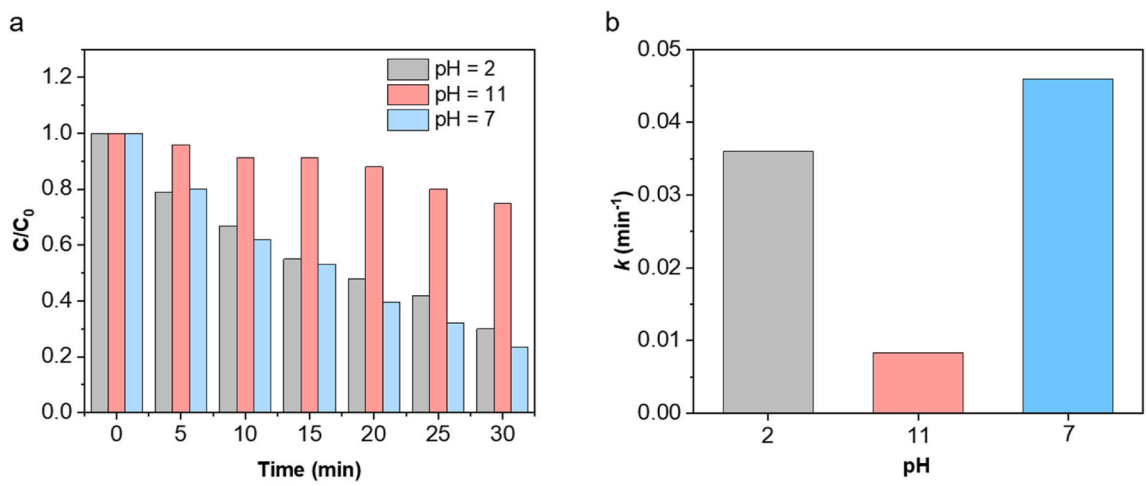


**Fig. 10.** Photocatalytic degradation of MB (a) and the rate constant for MB photodegradation (b) by $TiO_2$–N–$Ti_3C_2T_x$ at different pH.

photocatalytic applications, we coupled N–$Ti_3C_2T_x$ with $TiO_2$ and the resulting hybrid was used in the photocatalytic degradation of $NO_x$. The activity of $TiO_2$–N–$Ti_3C_2T_x$ was evaluated by NO conversion and $NO_x$ storage selectivity (Fig. 11a) and DeNOx index (Fig. 11b) and compared to pristine $TiO_2$ and $TiO_2$-M-$Ti_3C_2T_x$. $TiO_2$ exhibited reasonable NO conversion (53%), but produced massive amount of $NO_2$ with low $NO_x$ storage selectivity (58%) and a negative $DeNO_x$ index (−0.101), in agreement with previous reports [71–73]. In other words, $TiO_2$ oxidizes NO to $NO_2$ but fails to further oxidize $NO_2$ to other less toxic compounds such as nitrate and nitrite. Due to the high amount of $NO_2$ produced by $TiO_2$ and the higher toxicity of $NO_2$ than NO, it is apparent that $TiO_2$ is an ineffective photocatalyst for $NO_x$ abatement. $NO_x$ storage selectivity and $DeNO_x$ index achieved by $TiO_2$-M-$Ti_3C_2T_x$ were 62 and -0.055, respectively, indicating the inadequacy of utilizing $TiO_2$-M-$Ti_3C_2T_x$ in

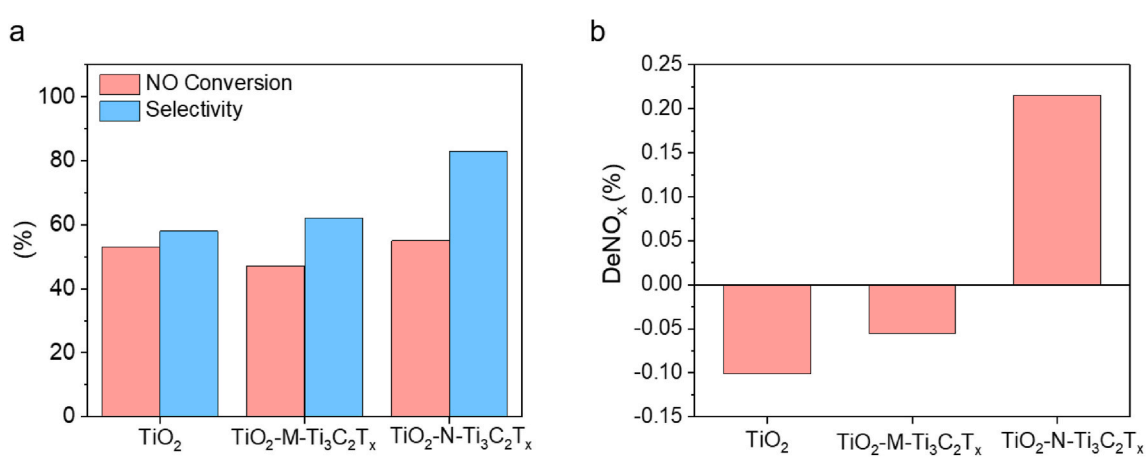


**Fig. 11.** NO conversion and $NO_x$ storage selectivity (a) and $DeNO_x$ index (b) for $TiO_2$, $TiO_2$-M-$Ti_3C_2T_x$, and $TiO_2$–N–$Ti_3C_2T_x$.

photocatalytic $NO_x$ oxidation. In contrast, $TiO_2$–N–$Ti_3C_2T_x$ exhibited high $NO_x$ abatement performance, with very high $NO_x$ storage selectivity (85%) and a positive $DeNO_x$ index (0.215) while maintaining the same NO conversion (55%). The high photocatalytic $NO_x$ removal achieved by $TiO_2$–N–$Ti_3C_2T_x$ is attributed to the high photon-$TiO_2$ interaction and the reduced electron-hole recombination in $TiO_2$–N–$Ti_3C_2T_x$. It is noteworthy that recent studies dealing with gas sensor fabrication suggested that $NO_x$ adsorbs effectively on oxygen-contain groups of MXene, where it can be stored in the form of other less toxic compounds (i.e. nitrite) [74,75]. Hence, it is reasonable to hypothesize that the abundant oxygen-containing groups available on N–$Ti_3C_2T_x$ provide adoption sites for $NO_x$ in $TiO_2$–N–$Ti_3C_2T_x$, enabling the removal of $NO_x$ through a non-photocatalytic route as well.

### 3.5. Charge carrier dynamics and photocatalytic activity of $TiO_2$–N–$Ti_3C_2T_x$ and $TiO_2$-M-$Ti_3C_2T_x$

A schematic illustrations of charge carrier dynamics in $TiO_2$–N–$Ti_3C_2T_x$ and $TiO_2$-M-$Ti_3C_2T_x$ and subsequent removal of MB and $NO_x$ are illustrated in Fig. 12a and b. It is well known the conduction band (CB) and valence band (VB) of $TiO_2$ are located at −0.29 and 2.91 eV (vs. normal hydrogen electrode), respectively. For $Ti_3AlC_2$, the valance state which is located below the Fermi level ($E_F$) is split into two sub-bands: (1) Ti 3d-Al 3p orbital close to the $E_F$ (Band I) and (2) the hybridized Ti 3d-Al 3s and Ti 3d-C 2p orbitals (Band II). After Al etching from $Ti_3AlC_2$ and the formation of $Ti_3C_2T_x$, Band II is dominated by Ti 3d and C 2p, and linked to Band I. Therefore, the weaker Ti–O coupling in energy state II results in the metallic phase of $Ti_3C_2T_x$ [2].

$Ti_3C_2T_x$ has a $E_F$ of −0.04 eV with high density of free carriers ($8 \pm 3 \times 10^{21}$ $cm^{-3}$) and electrical conductivity ($4600 \pm 1100$ S $cm^{-1}$). Consequently, the energy level of CB of $TiO_2$ is more negative than the Fermi level of $Ti_3C_2T_x$, making it possible for photoexcited electrons to travel from CB of $TiO_2$ to $Ti_3C_2T_x$, leaving holes in VB. In contrast to $TiO_2$-M-$Ti_3C_2T_x$, the concentration of electron-hole pairs is high in $TiO_2$–N–$Ti_3C_2T_x$ due to the high transparency of N–$Ti_3C_2T_x$ and the intimate interfacial contact between $TiO_2$ and N–$Ti_3C_2T_x$. Electrons and holes react with oxygen and water molecules, respectively, to form •OH radicals (most active ROS in MB and $NO_x$ degradation) and • $O_2^-$ radicals that are also capable of degrading MB and $NO_x$ pollutants. This phenomenon is robust in $TiO_2$–N–$Ti_3C_2T_x$ due to the intimate interfacial contact between $TiO_2$ and N–$Ti_3C_2T_x$. Also, the abundant oxygen-containing terminals on N–$Ti_3C_2T_x$ in $TiO_2$–N–$Ti_3C_2T_x$ can act as adsorption sites to facilitate the non-photocatalytic removal of MB and $NO_x$.

## 4. Conclusions

We have successfully fabricated N–$Ti_3C_2T_x$ with high transparency and abundant = O and –OH terminals using TPAOH as an exfoliating and fluorine-reducing agent. Coupling $TiO_2$ and N–$Ti_3C_2T_x$ results in a hybrid catalyst with unique morphology and surface chemistry, as well as outstanding photocatalytic activity in liquid and gas phases. The photocatalytic performances achieved by $TiO_2$–N–$Ti_3C_2T_x$ in liquid phase and gas phase reactions are superior to those of other well-known $TiO_2$–$Ti_3C_2T_x$ hybrids. Results show that due to the small size and high transparency of N–$Ti_3C_2T_x$, it exhibits intimate interfacial contact with $TiO_2$ that enables effective electron-hole separation without interrupting photon flux to $TiO_2$. In addition, the unique surface chemistry of N–$Ti_3C_2T_x$ facilitates efficient pollutant adsorption. Our findings show that N–$Ti_3C_2T_x$ is a promising and high-performance cocatalyst with $TiO_2$. Therefore, the utilization of N–$Ti_3C_2T_x$ as an alternative cocatalyst to conventional $Ti_3C_2T_x$ would enable the outstanding properties of MXenes to be fully exploited in photocatalysis.

## CRediT authorship contribution statement

Ahmed Al Mayyahi: Methodology, Investigation, Data curation, Formal analysis, Writing – original draft. Swagotom Sarker: Methodology, Supervision, Writing – review & editing. Brian M. Everhart: Resources. Bade Tonyali: Investigation. Umut Yucel: Investigation.

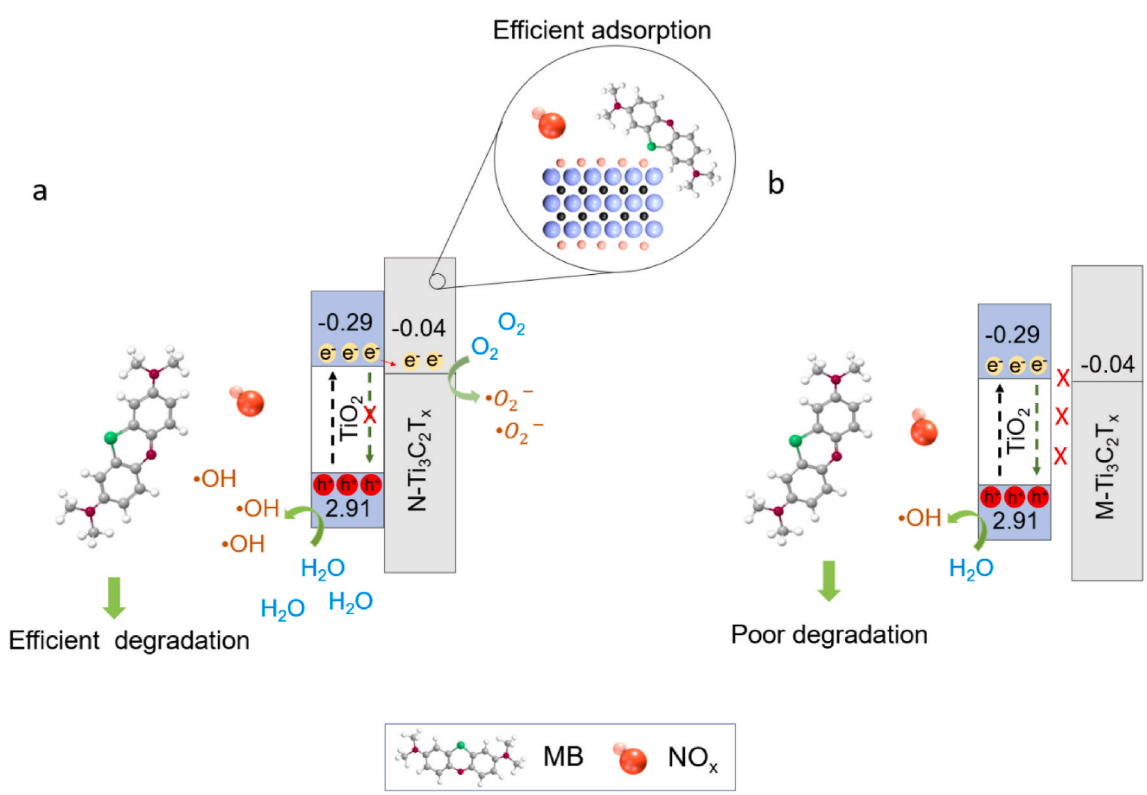


**Fig. 12.** Schematic illustration of charge carrier dynamics and removal of MB and $NO_x$ on $TiO_2$–N–$Ti_3C_2T_x$ (a) and $TiO_2$-M-$Ti_3C_2T_x$ (b) hybrid photocatalysts.

Placidus Amama: Supervision, Conceptualization, Formal analysis, Resources, Funding acquisition, Writing – review & editing.

## Declaration of competing interest

The authors declare that they have no known competing financial interests or personal relationships that could have appeared to influence the work reported in this paper.

## Data availability

Data will be made available on request.

## Acknowledgements

This study was supported by the National Science Foundation under the NSF CAREER program (Grant No. 1653527).

## Appendix A. Supplementary data

Supplementary data to this article can be found online at https://doi.org/10.1016/j.jpcs.2022.110875.

## References

[1] M. Naguib, M. Kurtoglu, V. Presser, J. Lu, J. Niu, M. Heon, L. Hultman, Y. Gogotsi, M.W. Barsoum, Two-dimensional nanocrystals produced by exfoliation of $Ti_3AlC_2$, Adv. Mater. 23 (2011) 4248–4253.
[2] H. Wang, Y. Wu, T. Xiao, X. Yuan, G. Zeng, W. Tu, S. Wu, H.Y. Lee, Y.Z. Tan, J. W. Chew, Formation of quasi-core-shell $In_2S_3$/anatase $TiO_2$@metallic $Ti_3C_2T_x$ hybrids with favorable charge transfer channels for excellent visible-light-photocatalytic performance, Appl. Catal. B Environ. 233 (2018) 213–225.
[3] T. Cai, L. Wang, Y. Liu, S. Zhang, W. Dong, H. Chen, X. Yi, J. Yuan, X. Xia, C. Liu, S. Luo, $Ag_3PO_4/Ti_3C_2$ MXene interface materials as a Schottky catalyst with enhanced photocatalytic activities and anti-photocorrosion performance, Appl. Catal. B Environ. 239 (2018) 545–554.
[4] M. Ye, X. Wang, E. Liu, J. Ye, D. Wang, Boosting the photocatalytic activity of P25 for carbon dioxide reduction by using a surface-alkalinized titanium carbide MXene as cocatalyst, ChemSusChem 11 (2018) 1606–1611.
[5] N. My Tran, Q. Thanh Hoai Ta, A. Sreedhar, J.-S. Noh, $Ti_3C_2T_x$ MXene playing as a strong methylene blue adsorbent in wastewater, Appl. Surf. Sci. 537 (2021), 148006.
[6] Z. Li, H. Zhang, L. Wang, X. Meng, J. Shi, C. Qi, Z. Zhang, L. Feng, C. Li, 2D/2D BiOBr/$Ti_3C_2$ heterojunction with dual applications in both water detoxification and water splitting, J. Photochem. Photobiol. Chem. 386 (2020), 112099.
[7] Y. Wang, X. Wang, Y. Ji, R. Bian, J. Li, X. Zhang, J. Tian, Q. Yang, F. Shi, $Ti_3C_2$ MXene coupled with CdS nanoflowers as 2D/3D heterostructures for enhanced photocatalytic hydrogen production activity, Int. J. Hydrogen Energy 47 (52) (2022) 22045–22053.
[8] C. Zhao, X. Yang, C. Han, J. Xu, Sacrificial agent-free photocatalytic oxygen evolution from water splitting over $Ag_3PO_4$/MXene hybrids, Solar RRL 4 (2020), 1900434.
[9] C. Hao, Y. Liao, Y. Wu, Y. An, J. Lin, Z. Gu, M. Jiang, S. Hu, X. Wang, $RuO_2$-loaded $TiO_2$–MXene as a high performance photocatalyst for nitrogen fixation, J. Phys. Chem. Solid. 136 (2020), 109141.
[10] C. Sun, Z. Chen, J. Cui, K. Li, H. Qu, H. Xie, Q. Zhong, Site-exposed $Ti_3C_2$ MXene anchored in N-defect g-$C_3N_4$ heterostructure nanosheets for efficient photocatalytic N2 fixation, Catal. Sci. Technol. 11 (2021) 1027–1038.
[11] I.A. Alsafari, S. Munir, S. Zulfiqar, M.S. Saif, M.F. Warsi, M. Shahid, Synthesis, characterization, photocatalytic and antibacterial properties of copper Ferrite/MXene ($CuFe_2O_4/Ti_3C_2$) nanohybrids, Ceram. Int. 47 (2021) 28874–28883.
[12] J. Ran, G. Gao, F.-T. Li, T.-Y. Ma, A. Du, S.-Z. Qiao, $Ti_3C_2$ MXene co-catalyst on metal sulfide photo-absorbers for enhanced visible-light photocatalytic hydrogen production, Nat. Commun. 8 (2017), 13907.
[13] C. Peng, X. Yang, Y. Li, H. Yu, H. Wang, F. Peng, Hybrids of two-dimensional Ti3C2 and TiO2 exposing {001} facets toward enhanced photocatalytic activity, ACS Appl. Mater. Interfaces 8 (2016) 6051–6060.
[14] W. Yuan, L. Cheng, Y. Zhang, H. Wu, S. Lv, L. Chai, X. Guo, L. Zheng, 2D-Layered carbon/$TiO_2$ hybrids derived from $Ti_3C_2$ MXenes for photocatalytic hydrogen evolution under visible light irradiation, Adv. Mater. Interfac. 4 (2017), 1700577.
[15] A. Shahzad, K. Rasool, M. Nawaz, W. Miran, J. Jang, M. Moztahida, K. A. Mahmoud, D.S. Lee, Heterostructural $TiO_2/Ti_3C_2$Tx (MXene) for photocatalytic degradation of antiepileptic drug carbamazepine, Chem. Eng. J. 349 (2018) 748–755.
[16] S. Sukidpaneenid, C. Chawengkijwanich, C. Pokhum, T. Isobe, P. Opaprakasit, P. Sreearunothai, Multi-function adsorbent-photocatalyst MXene-$TiO_2$ composites for removal of enrofloxacin antibiotic from water, J. Environ. Sci. 124 (2023) 414–428.
[17] N. My Tran, Q. Thanh Hoai Ta, J.-S. Noh, Unusual synthesis of safflower-shaped $TiO_2/Ti_3C_2$ heterostructures initiated from two-dimensional $Ti_3C_2$ MXene, Appl. Surf. Sci. 538 (2021), 148023.
[18] J. Chen, H. Zheng, Y. Zhao, M. Que, X. Lei, K. Zhang, Y. Luo, Preparation of facet exposed $TiO_2/Ti_3C_2T_x$ composites with enhanced photocatalytic activity, J. Phys. Chem. Solid. 145 (2020), 109565.
[19] K. Hantanasirisakul, M.-Q. Zhao, P. Urbankowski, J. Halim, B. Anasori, S. Kota, C. E. Ren, M.W. Barsoum, Y. Gogotsi, Fabrication of $Ti_3C_2T_x$ MXene transparent thin films with tunable optoelectronic properties, Adv. Electron. Mater. 2 (2016), 1600050.
[20] J. Halim, M.R. Lukatskaya, K.M. Cook, J. Lu, C.R. Smith, L.-Å. Näslund, S.J. May, L. Hultman, Y. Gogotsi, P. Eklund, M.W. Barsoum, Transparent conductive two-dimensional titanium carbide epitaxial thin films, Chem. Mater. 26 (2014) 2374–2381.
[21] P. Zhang, M. Xiang, H. Liu, C. Yang, S. Deng, Novel two-dimensional magnetic titanium carbide for methylene blue removal over a wide pH range: insight into removal performance and mechanism, ACS Appl. Mater. Interfaces 11 (2019) 24027–24036.
[22] H. Lei, Z. Hao, K. Chen, Y. Chen, J. Zhang, Z. Hu, Y. Song, P. Rao, Q. Huang, Insight into adsorption performance and mechanism on efficient removal of methylene blue by accordion-like $V_2CT_x$ MXene, J. Phys. Chem. Lett. 11 (2020) 4253–4260.
[23] Q. Zhang, J. He, X. Fu, S. Xie, R. Fan, H. Lai, W. Cheng, P. Ji, J. Sheng, Q. Liao, W. Zhu, H. Li, Fluorine-free strategy for hydroxylated $Ti_3C_2/Ti_3AlC_2$ catalysts with enhanced aerobic oxidative desulfurization and mechanism, Chem. Eng. J. 430 (2022), 132950.
[24] A.D. Dillon, M.J. Ghidiu, A.L. Krick, J. Griggs, S.J. May, Y. Gogotsi, M.W. Barsoum, A.T. Fafarman, Highly conductive optical quality solution-processed films of 2D titanium carbide, Adv. Funct. Mater. 26 (2016) 4162–4168.
[25] H.-i. Kim, G.-h. Moon, D. Monllor-Satoca, Y. Park, W. Choi, Solar photoconversion using graphene/$TiO_2$ composites: nanographene shell on $TiO_2$ core versus $TiO_2$ nanoparticles on graphene sheet, J. Phys. Chem. C 116 (2012) 1535–1543.
[26] M. Ghidiu, M.R. Lukatskaya, M.-Q. Zhao, Y. Gogotsi, M.W. Barsoum, Conductive two-dimensional titanium carbide 'clay' with high volumetric capacitance, Nature 516 (2014) 78–81.
[27] M. Alhabeb, K. Maleski, B. Anasori, P. Lelyukh, L. Clark, S. Sin, Y. Gogotsi, Guidelines for synthesis and processing of two-dimensional titanium carbide ($Ti_3C_2T_x$ MXene), Chem. Mater. 29 (2017) 7633–7644.
[28] J.S. Lee, K.H. You, C.B. Park, Highly photoactive, low bandgap $TiO_2$ nanoparticles wrapped by graphene, Adv. Mater. 24 (2012) 1084–1088.
[29] E. Ramos-Moore, P. Ferrari, D.E. Diaz-Droguett, D. Lederman, J.T. Evans, Raman and x-ray photoelectron spectroscopy study of ferroelectric switching in Pb(Nb,Zr,Ti)$O_3$ thin films, J. Appl. Phys. 111 (2012), 014108.
[30] A.A. Mayyahi, S. Sarker, B.M. Everhart, X. He, P.B. Amama, One-step fluorine-free synthesis of delaminated, OH-terminated $Ti_3C_2$: high photocatalytic $NO_x$ storage selectivity enabled by coupling $TiO_2$ and $Ti_3C_2$-OH, Mater. Today Commun. (2022), 103835.
[31] B.M. Everhart, B. McAuley, A. Al Mayyahi, B. Tonyali, U. Yucel, P.B. Amama, Photocatalytic $NO_x$ mitigation under relevant conditions using carbon nanotube-modified titania, Chem. Eng. J. 446 (2022), 136984.
[32] M.J. Friedrich, Air pollution is greatest environmental threat to health, JAMA 319 (2018) 1085.
[33] T. Zhang, L. Pan, H. Tang, F. Du, Y. Guo, T. Qiu, J. Yang, Synthesis of two-dimensional $Ti_3C_2T_x$ MXene using HCl+LiF etchant: enhanced exfoliation and delamination, J. Alloys Compd. 695 (2017) 818–826.
[34] Y. Xia, T.S. Mathis, M.-Q. Zhao, B. Anasori, A. Dang, Z. Zhou, H. Cho, Y. Gogotsi, S. Yang, Thickness-independent capacitance of vertically aligned liquid-crystalline MXenes, Nature 557 (2018) 409–412.
[35] P. Yan, R. Zhang, J. Jia, C. Wu, A. Zhou, J. Xu, X. Zhang, Enhanced supercapacitive performance of delaminated two-dimensional titanium carbide/carbon nanotube composites in alkaline electrolyte, J. Power Sources 284 (2015) 38–43.
[36] C. Zhao, Q. Wang, H. Zhang, S. Passerini, X. Qian, Two-dimensional titanium carbide/RGO composite for high-performance supercapacitors, ACS Appl. Mater. Interfaces 8 (2016) 15661–15667.
[37] C. Peng, P. Wei, X. Chen, Y. Zhang, F. Zhu, Y. Cao, H. Wang, H. Yu, F. Peng, A hydrothermal etching route to synthesis of 2D MXene ($Ti_3C_2$, $Nb_2C$): enhanced exfoliation and improved adsorption performance, Ceram. Int. 44 (2018) 18886–18893.
[38] H. Wang, Y. Wu, J. Zhang, G. Li, H. Huang, X. Zhang, Q. Jiang, Enhancement of the electrical properties of MXene $Ti_3C_2$ nanosheets by post-treatments of alkalization and calcination, Mater. Lett. 160 (2015) 537–540.
[39] S. Nam, S. Umrao, S. Oh, K.H. Shin, H.S. Park, I.-K. Oh, Sonochemical self-growth of functionalized titanium carbide nanorods on $Ti_3C_2$ nanosheets for high capacity anode for lithium-ion batteries, Compos. B Eng. 181 (2020), 107583.
[40] M. Naguib, O. Mashtalir, M.R. Lukatskaya, B. Dyatkin, C. Zhang, V. Presser, Y. Gogotsi, M.W. Barsoum, One-step synthesis of nanocrystalline transition metal oxides on thin sheets of disordered graphitic carbon by oxidation of MXenes, Chem. Commun. 50 (2014) 7420–7423.
[41] D.B. Lioi, G. Neher, J.E. Heckler, T. Back, F. Mehmood, D. Nepal, R. Pachter, R. Vaia, W.J. Kennedy, Electron-withdrawing effect of native terminal groups on the lattice structure of $Ti_3C_2T_x$ MXenes studied by resonance Raman scattering: implications for embedding MXenes in electronic composites, ACS Appl. Nano Mater. 2 (2019) 6087–6091.
[42] A. Sarycheva, Y. Gogotsi, Raman spectroscopy analysis of the structure and surface chemistry of $Ti_3C_2T_x$ MXene, Chem. Mater. 32 (2020) 3480–3488.
[43] R. Liu, W. Li, High-thermal-stability and high-thermal-conductivity $Ti_3C_2T_x$ MXene/poly(vinyl alcohol) (PVA) composites, ACS Omega 3 (2018) 2609–2617.

[44] T. Hu, J. Wang, H. Zhang, Z. Li, M. Hu, X. Wang, Vibrational properties of $Ti_3C_2$ and $Ti_3C_2T_2$ (T = O, F, OH) monosheets by first-principles calculations: a comparative study, Phys. Chem. Chem. Phys. 17 (2015) 9997–10003.
[45] A. Sarycheva, T. Makaryan, K. Maleski, E. Satheeshkumar, A. Melikyan, H. Minassian, M. Yoshimura, Y. Gogotsi, Two-dimensional titanium carbide (MXene) as surface-enhanced Raman scattering substrate, J. Phys. Chem. C 121 (2017) 19983–19988.
[46] S.A. Shah, T. Habib, H. Gao, P. Gao, W. Sun, M.J. Green, M. Radovic, Template-free 3D titanium carbide ($Ti_3C_2T_x$) MXene particles crumpled by capillary forces, Chem. Commun. 53 (2017) 400–403.
[47] Y. He, L. Wang, X. Wang, C. Shen, Q. Hu, A. Zhou, X. Liu, Surface reformation of 2D MXene by in situ $LaF_3$-decorated and enhancement of energy storage in lithium-ion batteries, J. Mater. Sci. Mater. Electron. 31 (2020) 6735–6743.
[48] J. Halim, K.M. Cook, M. Naguib, P. Eklund, Y. Gogotsi, J. Rosen, M.W. Barsoum, X-ray photoelectron spectroscopy of select multi-layered transition metal carbides (MXenes), Appl. Surf. Sci. 362 (2016) 406–417.
[49] J. Halim, I. Persson, E.J. Moon, P. Kühne, V. Darakchieva, P.O.Å. Persson, P. Eklund, J. Rosen, M.W. Barsoum, Electronic and optical characterization of 2D $Ti_2C$ and $Nb_2C$ (MXene) thin films, J. Phys. Condens. Matter 31 (2019), 165301.
[50] H.-W. Tien, Y.-L. Huang, S.-Y. Yang, J.-Y. Wang, C.-C.M. Ma, The production of graphene nanosheets decorated with silver nanoparticles for use in transparent, conductive films, Carbon 49 (2011) 1550–1560.
[51] G. Zorn, L.-H. Liu, L. Árnadóttir, H. Wang, L.J. Gamble, D.G. Castner, M. Yan, X-Ray photoelectron spectroscopy investigation of the nitrogen species in photoactive perfluorophenylazide-modified surfaces, J. Phys. Chem. C 118 (2014) 376–383.
[52] G. Liu, C. Han, M. Pelaez, D. Zhu, S. Liao, V. Likodimos, N. Ioannidis, A.G. Kontos, P. Falaras, P.S.M. Dunlop, J.A. Byrne, D.D. Dionysiou, Synthesis, characterization and photocatalytic evaluation of visible light activated C-doped $TiO_2$ nanoparticles, Nanotechnology 23 (2012), 294003.
[53] V. Schier, H.J. Michel, J. Halbritter, ARXPS-analysis of sputtered TiC, SiC and $Ti_{0.5}Si_{0.5}C$ layers, Fresen. J. Anal. Chem. 346 (1993) 227–232.
[54] Y. Huang, D. Chen, X. Hu, Y. Qian, D. Li, Preparation of $TiO_2$/carbon nanotubes/reduced graphene oxide composites with enhanced photocatalytic activity for the degradation of rhodamine B, Nanomaterials 8 (2018).
[55] Y. Li, Z. Wang, X.-J. Lv, N-doped $TiO_2$ nanotubes/N-doped graphene nanosheets composites as high performance anode materials in lithium-ion battery, J. Mater. Chem. 2 (2014) 15473–15479.
[56] A. Al Mayyahi, B.M. Everhart, T.B. Shrestha, T.C. Back, P.B. Amama, Enhanced charge separation in $TiO_2$/nanocarbon hybrid photocatalysts through coupling with short carbon nanotubes, RSC Adv. 11 (2021) 11702–11713.
[57] M. Cao, F. Wang, L. Wang, W. Wu, W. Lv, J. Zhu, Room temperature oxidation of $Ti_3C_2$MXene for supercapacitor electrodes, J. Electrochem. Soc. 164 (2017) A3933–A3942.
[58] H. Liu, S. Liu, Z. Zhang, X. Dong, T. Liu, Hydrothermal etching fabrication of $TiO_2$@graphene hollow structures: mutually independent exposed {001} and {101} facets nanocrystals and its synergistic photocaltalytic effects, Sci. Rep. 6 (2016), 33839.
[59] B. Liu, Y. Huang, Y. Wen, L. Du, W. Zeng, Y. Shi, F. Zhang, G. Zhu, X. Xu, Y. Wang, Highly dispersive {001} facets-exposed nanocrystalline $TiO_2$ on high quality graphene as a high performance photocatalyst, J. Mater. Chem. 22 (2012) 7484–7491.
[60] S.P. Lim, A. Pandikumar, H.N. Lim, R. Ramaraj, N.M. Huang, Boosting photovoltaic performance of dye-sensitized solar cells using silver nanoparticle-decorated N,S-Co-Doped-$TiO_2$ photoanode, Sci. Rep. 5 (2015), 11922.
[61] Y. Nosaka, A. Nosaka, Understanding hydroxyl radical (•OH) generation processes in photocatalysis, ACS Energy Lett. 1 (2016) 356–359.
[62] H. Huang, Y. Song, N. Li, D. Chen, Q. Xu, H. Li, J. He, J. Lu, One-step in-situ preparation of N-doped $TiO_2$@C derived from $Ti_3C_2$ MXene for enhanced visible-light driven photodegradation, Appl. Catal. B Environ. 251 (2019) 154–161.
[63] X. Wang, Z. Xu, M. Rommel, B. Dong, L. Song, C.A.T.H. Tee, F. Fang, Electron paramagnetic resonance characterization of aluminum ion implantation-induced defects in 4H-SiC, Nanotechnol. Precis. Eng. 2 (2019) 157–162.
[64] V. Natu, R. Pai, O. Wilson, E. Gadasu, H. Badr, A. Karmakar, A.J.D. Magenau, V. Kalra, M.W. Barsoum, Effect of base/nucleophile treatment on interlayer ion intercalation, surface terminations, and osmotic swelling of $Ti_3C_2T_z$ MXene multilayers, Chem. Mater. 34 (2) (2022) 678–693.
[65] M. Kalapsazova, R. Stoyanova, E. Zhecheva, G. Tyuliev, D. Nihtianova, Sodium deficient nickel–manganese oxides as intercalation electrodes in lithium ion batteries, J. Mater. Chem. 2 (2014) 19383–19395.
[66] B.-M. Jun, S. Kim, H. Rho, C.M. Park, Y. Yoon, Ultrasound-assisted $Ti_3C_2T_x$ MXene adsorption of dyes: removal performance and mechanism analyses via dynamic light scattering, Chemosphere 254 (2020), 126827.
[67] Y. Nakabayashi, Y. Nosaka, The pH dependence of OH radical formation in photo-electrochemical water oxidation with rutile $TiO_2$ single crystals, Phys. Chem. Chem. Phys. 17 (2015) 30570–30576.
[68] F. Wu, W. Liu, J. Qiu, J. Li, W. Zhou, Y. Fang, S. Zhang, X. Li, Enhanced photocatalytic degradation and adsorption of methylene blue via $TiO_2$ nanocrystals supported on graphene-like bamboo charcoal, Appl. Surf. Sci. 358 (2015) 425–435.
[69] S. Wardiayati, S.H. Dewi, Influence of $Fe_3O_4$ addition in $TiO_2$ catalyst on the degradation process of methylene blue, J. Phys. Conf. 1091 (2018), 012015.
[70] L. Zhang, D. Huang, P. Zhao, G. Yue, L. Yang, W. Dan, Highly efficient methylene blue removal by TMAOH delaminated $Ti_3C_2T_x$ MXene suspension and the mechanistic aspect, Separ. Purif. Technol. 288 (2022), 120718.
[71] M. Balci Leinen, D. Dede, M.U. Khan, M. Çağlayan, Y. Koçak, H.V. Demir, E. Ozensoy, CdTe quantum dot-functionalized P25 titania composite with enhanced photocatalytic $NO_2$ storage selectivity under UV and vis irradiation, ACS Appl. Mater. Interfaces 11 (2019) 865–879.
[72] M. Çağlayan, M. Irfan, K.E. Ercan, Y. Kocak, E. Ozensoy, Enhancement of photocatalytic $NO_x$ abatement on titania via additional metal oxide $NO_x$-storage domains: interplay between surface acidity, specific surface area, and humidity, Appl. Catal. B Environ. 263 (2020), 118227.
[73] L. Yang, A. Hakki, F. Wang, D.E. Macphee, Different roles of water in photocatalytic $DeNO_x$ mechanisms on $TiO_2$: basis for engineering nitrate selectivity? ACS Appl. Mater. Interfaces 9 (2017) 17034–17041.
[74] S.J. Kim, H.-J. Koh, C.E. Ren, O. Kwon, K. Maleski, S.-Y. Cho, B. Anasori, C.-K. Kim, Y.-K. Choi, J. Kim, Y. Gogotsi, H.-T. Jung, Metallic $Ti_3C_2T_x$ MXene gas sensors with ultrahigh signal-to-noise ratio, ACS Nano 12 (2018) 986–993.
[75] Y. Zhang, Y. Jiang, Z. Duan, Q. Huang, Y. Wu, B. Liu, Q. Zhao, S. Wang, Z. Yuan, H. Tai, Highly sensitive and selective $NO_2$ sensor of alkalized $V_2CT_x$ MXene driven by interlayer swelling, Sensor. Actuator. B Chem. 344 (2021), 130150.